Colored oxides with hibonite structure II[§]: Structural and optical properties of $CaAl_{12}O_{19}$-type pigments with chromophores based on Fe, Mn, Cr and Cu

Elena A. Medina, Jun Li*, M. A. Subramanian

Department of Chemistry, Oregon State University, Corvallis, Oregon 97331, United States

Abstract

Colored hibonite-type oxides with a general formula $CaAl_{12-x}M_xO_{19}$ were prepared by solid state reactions through M-site substitution of aluminum with various di-, tri- and tetravalent cations (*M* = Fe, Mn, Cr, Cu, Ga, In, Ti, Ge, Sn or any combination thereof), where Fe, Mn, Cr and Cu are chromophore ions. Neutron Rietveld refinements of $CaAl_{9.5}Fe_{2.5}O_{19}$, $CaAl_{11.5}Mn_{0.5}O_{19}$ and $CaAl_{10}SnMnO_{19}$ compounds show that Fe^{3+} and Mn^{2+} prefer to occupy the tetrahedral site, while Mn^{3+} has an evident preference for both tetrahedral and octahedral sites and Sn^{4+} for octahedral site in the hibonite structure. No oxygen vacancies are found by structural analyses, and magnetic measurement confirms divalent Mn for $CaAl_{11}Sn_{0.5}Mn_{0.5}O_{19}$ and trivalent Mn for $CaAl_{11.5}Mn_{0.5}O_{19}$. Diffuse reflectance spectra reveal that the d-d transitions occurring in transition metal chromophores are mainly responsible for the observed colors. The colored powders exhibit fairly high reflectance in the near-infrared region (750–2500 nm) which makes them potential candidates for cool pigment applications. Synthesis and characterization methods are briefly reviewed for hibonite type of oxides, especially those containing Fe, Mn, Cr and Cu.

Keywords: Hibonite, Colored oxides, Neutron diffraction, Optical properties, Cool pigments

§ Part I was published in *Progress in Solid State Chemistry* 44 (2016) 107–122 with the title "Colored oxides with hibonite structure: A potential route to non-cobalt blue pigments".

* Corresponding author.

E-mail address: lijun@oregonstate.edu (J. Li)

Contents

1. Introduction

Hibonite is a family of metal oxides isostructural to magnetoplumbite [1-4]. Mineral hibonite is more often found in meteorites than on earth [5]. The natural and synthetic hibonites have been widely studied for their structural and magnetic properties and applications as phosphor and laser materials [6-10].

The ideal hibonite $CaAl_{12}O_{19}$ has a hexagonal unit cell and crystallizes in $P6_3/mmc$ space group where a = 5.5587(1) Å, c = 21.8929(3) Å, V = 585.84 Å^3 [11,12]. The crystal structure consists of two building blocks alternating along the c-axis (Fig. 1): the spinel layer (S-block) and the trigonal bipyramidal layer (R-block) [13-15]. Calcium ions occupy the 12-fold coordination sites within the R-blocks. There are five distinct crystallographic positions for Al^{3+} ions in this hexagonal structure: Al1: trigonal antiprismatic, coordination number (CN) = 6; Al2: trigonal bipyramidal (TBP, CN = 5); Al3: tetrahedral (CN = 4); Al4: face-shared octahedral (CN = 6); and Al5: edge-shared octahedral (CN = 6). This unique structural feature, in addition to the low cost of its chemical constituents, makes $CaAl_{12}O_{19}$ an attractive oxide host in search for new materials with interesting and applicable properties.

Hibonite-type compounds containing Fe, Mn, Cr and Cu have been reported mostly for their crystal structures and magnetic properties, their optical properties however are rarely investigated. X-ray [16-18] and neutron diffraction [19] were applied to refine the structures of $CaFe_6Al_6O_{19}$ [16], $SrAl_xFe_{12-x}O_{19}$ [17,18] and $BaFe_{12-x}Mn_xO_{19}$ [19] phases. The distribution of Mn and Fe ions in $BaFe_{12-x}Mn_xO_{19}$ [20], the site preference of Cr in $BaFe_{12-x}Cr_xO_{19}$ [21], the arrangement of Ti and Mn ions in $BaTiMnFe_{10}O_{19}$ [22] and Fe ions in $SrAl_xFe_{12-x}O_{19}$ [23] were also determined with diffraction methods. Structural, electrical and magnetic properties of $CaCr_xFe_{12-x}O_{19}$ (x = 3, 4, 8, 9) [24] and $CaFe_{12-x}Al_xO_{19}$ (x = 3, x = 4) [25] as well as relaxor-like improper ferroelectricity in $PbFe_6Ga_6O_{19}$ were studied [26]. Ahn et al. reported Mn-doped $CaAl_{12}O_{19}$ as phosphor materials in white organic light-emitting devices [27]. Iron-containing hibonites were widely explored as magnetic materials for permanent magnets, microwave and high-density magnetic recording devices [28]. The analysis of $BaAl_xFe_{12-x}O_{19}$ single crystals revealed a dependence of magnetic properties on concentration of aluminum in the solid solution [29]. Structural and spectroscopic properties of $LaAlFe_{11}O_{19}$, $SmFe_4Al_8O_{19}$ and $Eu_{0.83}Fe_2Al_{10}O_{19}$ phases were examined [30,31]. Ounnunkad et al. studied the effect of La doping on structural, magnetic and microstructural properties of $Ba_{1-x}La_xFe_{12}O_{19}$ ceramics and concluded that the saturation magnetization (M_s) increased with La content and reached to a maximum at x = 0.15 [32]. Magnetic measurement of $SrFe_{12-x}Al_xO_{19}$ nanoparticles by auto-combustion route demonstrated that Al^{3+} substitution affected the magnitude of M_s and coercivity (H_c) [33].

Although the color of ideal hibonite $CaAl_{12}O_{19}$ is white, it rarely forms without impurities in nature. A variety of colors have been reported for hibonite-bearing minerals [34-38]. Murchison meteorite found in 1969 in Australia contains "Blue Angel", a relatively large (~1.5 mm) hibonite-containing inclusion, and the brilliant blue color of which was ascribed to the presence of V^{3+} [39]. Burns proposed three mechanisms responsible for the blue color in natural meteoritic hibonite: 1) crystal field transitions within V^{3+} and Ti^{3+} located in the TBP sites; 2) charge transfer transitions from Fe^{2+} to Ti^{4+} in face-shared octahedra similar to that in sapphire;

3) color centers introduced when Al^{26} decays to Mg^{26} or trapped electrons in the lattice as a result of nonstoichiometry and structural defects [40]. The Fe-containing hibonite $(Fe,Mg)Al_{12}O_{19}$ was discovered in inclusion from the Allende meteorite [41]. Holtstam performed a Mössbauer spectroscopic study of iron in natural hibonite from Madagascar [42]. Synthetic hibonite-type oxides also show interesting colors upon various substitutions in different M-sites of $AM_{12}O_{19}$ hosts and the origin of the coloration has been explored experimentally. $LnMgAl_{11}O_{19}$ single crystals [43] were synthesized and characterized: $LaMgAl_{11}O_{19}$ and $GdMgAl_{11}O_{19}$ are colorless, $La_{1-x}Nd_xMgAl_{11}O_{19}$ is slightly mauve colored, $PrMgAl_{11}O_{19}$ is green, $NdMgAl_{11}O_{19}$ is purple, $SmMgAl_{11}O_{19}$ is ochre, and $EuMgAl_{11}O_{19}$ is slightly blue. The correlation between observed blue color and the amount of Ti^{3+} in Ti-containing $CaAl_{12}O_{19}$ solid solutions was examined and the concentration of Ti^{3+} was found to be associated with oxygen fugacity [44]. It was shown that depending on the amount and ratio of Ti^{3+} and Ti^{4+} ions, $CaAl_{12}O_{19}$-based crystals could be colorless, blue, greenish or orange [45]. Gasperin et al. studied the $LaM_xAl_{11}O_{18+x}$ (M = Mn, Co, Cu) series and found that Co-containing crystals were blue, $LaCu_xAl_{11}O_{19}$ was colorless and the green color of $LaMn_xAl_{11}O_{18+x}$ single crystals was due to Mn^{2+} ions [46]. $LaMAl_{11}O_{19}$ (M = Ni, Co, Fe, Mn) compounds were discovered to be blue with Ni substitution on Al site, dark blue with Co, pink with Fe, and green with Mn [47]. Originally colorless $La(Mg_{1-y}Mn_y)Al_{11}O_{18+x}$ (x, $y \leq 1$) crystals showed brownish coloration under UV and X-ray radiation exposure and defect centers were responsible for the color change [48]. The dark green color of $SrCr_9Ga_3O_{19}$ single crystals was due to the presence of Cr^{3+} ions on octahedral sites [49].

Recently colored oxides with hibonite structure have attracted attention as an appealing host for inorganic pigment design. There have been several reports on turquoise pigments with Ni^{2+} as a chromophore in tetrahedral coordination of $CaAl_{12}O_{19}$ [50-52]. Blue hibonite compounds based on tetrahedrally coordinated Co^{2+} have also been investigated [53], and Co- and Ni-containing solid wastes were proposed to be used as raw materials for pigment preparation [54,55]. We have discovered a series of hibonite-type pigments with intense royal blue colors [56] as well as many hibonite compositions with a variety of colors other than blue [57]. This work is mainly focused on syntheses and characterization of colored hibonite solid solutions and compositions with Fe, Mn, Cr and Cu as chromophores. A brief review will be given for other M-containing (M = Fe, Mn, Cr and Cu) hibonites.

We report here crystal structures, by X-ray and neutron powder diffraction, and optical properties of three solid solutions $CaAl_{12-x}Mn_xO_{19}$, $CaAl_{12-x}Fe_xO_{19}$ and $CaAl_{12-2x}Mn_xSn_xO_{19}$ along with some new hibonite compositions that exhibit colors other than blue. We expect our research will lead to routes for designing novel inorganic pigments that are durable, inexpensive, non-toxic and heat-reflective.

2. Materials and syntheses

2.1 Conventional solid state method

Conventional solid state synthesis is the most common way to prepare inorganic metal oxides, particularly in this work, colored oxides based on $CaAl_{12}O_{19}$ hibonite structure. All our samples were made using this method. Stoichiometric amounts of $CaCO_3$ (Sigma-Aldrich,

99.0%), Al_2O_3 (Cerac, 99.99%), Fe_2O_3 (Alfa Aesar, 99.945%), In_2O_3 (Aldrich, 99.99%), Cr_2O_3 (Alfa Aesar, 99.997%), Mn_2O_3 (Alfa Products, 98%), Ga_2O_3 (Aldrich, 99.99%), MnO (JMC, 99.5%), FeO (Alfa Aesar, 99.5%), TiO_2 (Aldrich, 99.9%), SnO_2 (JMC, 99.9%), GeO_2 (Cerac, 99.999%) and CuO (Alfa Aesar, 99.0%) were mixed and grounded using agate mortars with pestles. The powder mixture was pelletized and heated in alumina crucibles at 1400°C for 12 h in air; and the resulting pellets were then grounded and reheated at 1450°C for additional 12 h.

2.2 Other preparation methods

In addition to standard solid state synthesis [2,7,8,20,23,24,38,44,49,51-52,56] other preparation methods were also applied to obtain hibonite-type oxides. Solution combustion synthesis using metal nitrates was performed [25,32,50]. Powder samples were made through wet techniques: sol-gel [8,21] and hydrolysis of alkoxydes followed by thermal decomposition and reaction [8]. However, low temperature synthesis techniques are not always applicable for synthesis of hibonite phases because most of them require fairly high synthetic temperatures (above 1300°C).

Single crystals have been obtained by flux method [8,29,58] or by various high temperature techniques: flame fusion or Verneuil method [6,8,9,43,46,47], floating zone method [6,8,12,43,47] and Czochralski method [6,8,18,49,59,60].

3. Characterization

3.1 Techniques applied for hibonites

X-ray diffraction (XRD) was the most common technique applied for structure studies of hibonite-type single crystals and powder samples [1,3-6,8,12,14,16,18,23,37,44,49,50,51]. In some cases neutron Rietveld refinement was performed [2,3,19,20,22,44,56]. Chemical composition and surface topography of natural and prepared hibonite-type single crystals were obtained by scanning electron microscope method (SEM) [14,25,32,33,37,39,41,44,51,53,55]. Elemental distribution was studied by electron microprobe analysis (EMP) [3-5,41]. Spectroscopic investigations (absorbance and fluorescence spectra) [4,6,7,34,42,55], near-infrared (IR) spectra [7,37], emission spectra [9], luminescence [10], color description by $L^*a^*b^*$ parameters [53-55] and other optical property characterizations [34,35,41,43,50,51,53-55] were employed. Additional information of the hibonite-based oxides was collected using electron paramagnetic resonance (EPR) [7], Mössbauer technique [4,35,38,40,42-43], magnetic susceptibility measurements [6,21,56] magnetic structure refinement [19,29,33,47], thermal analysis [33,55], along with measurements of electrical properties [24,25], dielectric properties [56] chemical reactivity [43] and microhardness [43,47].

3.2 For colored hibonites in this work

XRD data were collected using a Rigaku MiniFlex II diffractometer with Cu Kα radiation (λ = 1.5418Å) and a graphite monochromator at room temperature. For phase identification the measurements were carried out at 0.5°/min within 15° to 70° 2θ range. Powder neutron diffraction data were collected on the 32-counter high-resolution diffractometer BT-1 at the

Center for Neutron Research at the National Institute of Standards and Technology. A Cu (311) monochromator, yielding a wavelength of 1.5403(2) Å, was employed. Collimation of 15′ of arc was used before the monochromator, 20′ before the sample, and 7′ before the detectors. The samples were loaded into vanadium containers of 15.6 mm diameter and 50 mm length. Data were collected at room temperature over a 2θ range of 3° to 167° for 5.5 hr. XRD and neutron data were refined using GSAS-EXPGUI software [61,62]. Bond-valence analysis of the neutron structures made use of the bond-valence calculator [63].

Konica Minolta CM-700d Spectrophotometer (Standard illuminant D_{65}) was used to measure *L**, *a**, *b** color coordinates. Diffuse reflectance data in the visible range were measured using a homemade UV-VIS spectrophotometer (MgO as the reference) and converted to absorbance using the Kubelka-Munk equation [64]. NIR reflectance data (up to 2500 nm) were collected using a Jasco V-670 Spectrophotometer.

Magnetic properties measurements were made using a Quantum Design Physical Property Measurement System (QD-PPMS) at temperature range of 5 K to 300 K (zero-field cooling, applied magnetic field 0.5 T). Inverse magnetic susceptibility data was used to fit for Curie-Weiss law. Diamagnetic corrections were made for calculations of experimental μ_B [65].

Dielectric properties measurements were performed on Dielectric instrument HP Precision LCR Meter 4284A (20 Hz – 1 MHz) in 25–250°C temperature range. Samples were pelletized and sintered at synthesis temperatures to obtain a theoretical density above 75%. The surface of the pellets was polished with sandpaper to achieve smoothness and even thickness, and both sides of the pellets were then painted with silver coating and dried in the oven overnight.

4. Results and discussion

4.1 Colors and phase analyses

Various substitutions were attempted on Al sites in $CaAl_{12}O_{19}$ host lattice with Fe, Mn, Cr and Cu as chromophores. To guarantee charge neutrality of the system heterovalent substitution for Al^{3+} ion can be achieved by combining divalent ions (M^{2+} = Fe, Mn, Cu) with tetravalent ions (M^{4+} = Ti, Sn, Ge) such that $M^{2+} + M^{4+} \rightarrow 2Al^{3+}$. Representative colors of the powder samples are demonstrated in Figures 2-4.

When Fe^{3+} is used as a chromophore, the color of $CaAl_{12-x}Fe_xO_{19}$ (x = 0.5–4.5) series (Fig. 2(a)) changes from yellow (x = 0.5) to red brown (x = 2.5) with increasing x, and it becomes even darker at higher Fe concentrations: reddish chocolate (x = 3.0) and dark chocolate (x = 3.5). The color evolution of $CaAl_{11-x}GaFe_xO_{19}$ (x = 0.5–2.5) series is similar to that of $CaAl_{12-x}Fe_xO_{19}$ but with darker colors (Fig. 2(b)): for instance when x = 2.0, $CaAl_{10}Fe_2O_{19}$ is dark orange brown while $CaAl_9GaFe_2O_{19}$ is dark brick red. When some di-, tri- and tetra-valent ions were added in coupled substitutions for charge compensation, Fe-containing hibonites show different colors (Fig. 2(c)) and Fe^{2+} is a chromophore ion in this case. Addition of Ti, Ge, Sn to $CaAl_{11.5}Fe_{0.5}O_{19}$ changes the color from sandy brown to greenish white, light olive or bright olive. Adding Cu^{2+} as a second chromophore to above series $CaAl_{11}Fe_{0.5}M_{0.5}O_{19}$ (M = Ti, Ge, Sn) results in slightly darker color, and further addition of In^{3+} or Ga^{3+} to $CaAl_{10.5}Fe_{0.5}Cu_{0.5}M_{0.5}O_{19}$ (M = Ti, Sn) makes the color even darker: $CaAl_{9.5}InSn_{0.5}Cu_{0.5}Fe_{0.5}O_{19}$ gives the most intense olive green. The color of $CaAl_{9.5}GaM_{0.5}Cu_{0.5}Fe_{0.5}O_{19}$ is olive green for M = Sn and yellowish olive for M = Ti. In

general, trivalent Fe^{3+} gives yellow to reddish brown colors while divalent Fe^{2+} results in green colors with yellowish hue.

When Mn plays a role of chromophore the color of $CaAl_{12-x}Mn_xO_{19}$ (x = 0.1–0.6) series varies from burlywood (x = 0.1) to saddle brown (x = 0.5) (Fig. 3(a)). Coupled substitution with Sn or Ti makes the colors of $CaAl_{12-x}Sn_xMn_xO_{19}$ (x = 0.1–1.0) (Fig. 3(b)) and $CaAl_{12-x}Ti_xMn_xO_{19}$ (x = 0.5, 1.0) become lighter, assuming divalent Mn^{2+} as the chromophore compared with trivalent Mn^{3+} in $CaAl_{12-x}Mn_xO_{19}$. Addition of Cu^{2+} to $CaAl_{11}Mn_{0.5}Sn_{0.5}O_{19}$ results in similar but slightly darker color (Fig. 3(c)). Adding In or Ga to $CaAl_{10.5}Mn_{0.5}Cu_{0.5}Sn_{0.5}O_{19}$ gives reddish or chocolate brown color darker than that of $CaAl_{11.5}Mn_{0.5}O_{19}$.

In the case of Cr-containing samples, the color of $CaAl_{12-x}Cr_xO_{19}$ (x = 0.5–3.5) series changes from light rosy brown (x = 0.5) to grayish green (x = 3.0) with increasing x (Fig. 4(a)). Co-doping $CaAl_{12-x}Cr_xO_{19}$ (x = 0.5) with Cu, Ga, Ti, Ge and Sn makes the sample color become darker (Fig. 4(b)). With addition of Cu and Sn $CaAl_{11.5}Cr_{0.5}O_{19}$ becomes tan; $CaAl_{10.5}Ge_{0.5}Cu_{0.5}Cr_{0.5}O_{19}$ and $CaAl_{9.5}GaSn_{0.5}Cu_{0.5}Cr_{0.5}O_{19}$ are rosy brown. In general, Sn gives lighter colors than Ti; In gives more brownish shades compared with Ga, and Ga-containing samples normally have a rosy brown hue.

When Cu is a chromophore coupled substitution with Ti produces creamy color for $CaAl_{11}Cu_{0.5}Ti_{0.5}O_{19}$ and golden brown color for $CaAl_{10}CuTiO_{19}$. The color of $CaAl_{11}Ge_{0.5}Cu_{0.5}O_{19}$ is extremely light turquoise and that of $CaAl_{11}Sn_{0.5}Cu_{0.5}O_{19}$ is light cyan.

Phase identification of powder samples was performed by X-ray diffraction. The solid solutions and compositions are summarized in Table 1 and XRD patterns are shown in Figures 5-12. As we can see, all samples are phase pure and crystallize in $P6_3/mmc$ hexagonal space group. Compounds prepared in the present work except $CaAl_{12-x}Fe_xO_{19}$ (x = 0.5–4.5) [66] are reported for the first time.

Cell parameters of $CaAl_{12-x}Fe_xO_{19}$ (x = 0.5–4.5) and $CaAl_{12-x}Cr_xO_{19}$ (x = 0.5–3.5) solid solutions are shown in Fig. 13. Shannon ionic radii of Fe^{3+} and Cr^{3+} are larger than that of Al^{3+} [67], hence as the Fe/Cr content increases a, c and V cell values also increase, confirming the formation of the solid solution. Cell c increases faster with increasing x than cell a due to the fact that layered hibonite structure is more susceptible to lattice variation, expansion or contraction, in the direction of c-axis.

Solid solution of $CaAl_{12-x}Mn_xO_{19}$ (x = 0.1–0.6) was only made phase pure up to x = 0.6 based on XRD analysis, and the actual solubility limit of Mn could be lower according to the neutron refinement (see Section 4.2). As a consequence, the change in cell a, c, V and c/a ratio with Mn substitution is not significant across the small range of x (Fig. 14). The distribution of Mn cations over different sites in the host lattice may also affect the magnitude of structural response upon substitution.

The impact of coupled substitution with Sn and Mn on cell a, c, V and c/a ratio is illustrated in Fig. 15 for $CaAl_{12-2x}Sn_xMn_xO_{19}$ (x = 0.1–1.0) series. The substantial cell expansion with increasing x is expected given the larger ionic radii of Mn^{2+} and Sn^{4+} compared with that of Al^{3+} [67]. The anisotropic lattice variation of $CaAl_{12-2x}Sn_xMn_xO_{19}$ upon substitution is more pronounced than that of $CaAl_{12-x}Fe_xO_{19}$ and $CaAl_{12-x}Cr_xO_{19}$ series as demonstrated by a conspicuous increase in c/a ratio and a more rapid increase of cell c than a.

The lattice parameters calculated by neutron Rietveld refinement are plotted in Figs.13–15 for comparison. The discrepancy between X-ray and neutron data is merely sample related. The samples sent for neutron experiments were heated for longer hours with more intermediate grindings, the slightly larger cell parameters shown by neutron samples thus indicating relatively higher level of substitution than samples examined by X-ray diffraction.

4.2 Crystal structures by neutron diffraction

Compared with X-ray diffraction, the neutron scattering power of oxygen is much greater and hence ensures more accurate determination of oxygen positions and stoichiometry. Furthermore, the neutron scattering lengths are 3.449 fm for Al, 9.45 fm for Fe, -3.73 fm for Mn and 6.225 fm for Sn, respectively [68]. The negative value for Mn vs the positive value for Sn is very beneficial in differentiating the scattering contributions of Mn and Sn. Rietveld refinements of neutron data were performed for $CaAl_{9.5}Fe_{2.5}O_{19}$, $CaAl_{11.5}Mn_{0.5}O_{19}$ and $CaAl_{10}SnMnO_{19}$ samples. The observed and calculated profiles are shown in Figs. 16–18, and the refinement results are summarized in Tables 2–6. More details are provided in Supporting Information as cif files.

All the data were refined in $P6_3/mmc$ space group with cations in trigonal bipyramidal (TBP) coordination being displaced off the center along the *c* axis (Fig.1, Al2 site). The application of split-atom model is not uncommon for cations with TBP symmetry in hibonite structure [12,18,46,56,69,70], and this cation displacement has been verified experimentally by ^{27}Al NMR studies and ^{57}Fe Mössbauer spectroscopy [56]. The refined distances between two split sites are 0.099 Å for $CaAl_{9.5}Fe_{2.5}O_{19}$, 0.398 Å for $CaAl_{11.5}Mn_{0.5}O_{19}$ and 0.408 Å for $CaAl_{10}SnMnO_{19}$, respectively (Table 6). In $CaAl_{12}O_{19}$, $SrAl_{12}O_{19}$ and $CaAl_{10}TiNiO_{19}$, these distances are 0.372 Å, 0.638 Å and 0.633 Å, respectively [56,69]. It is well known that cations at TBP (Al2) site of the hibonite structure are severely underbonded [69], with much longer Al2–O apical distances than basal plane distances. Low bond valence sums (BVS) of the cation at Al2 site could be the driving force of moving it off the ideal site (0,0,1/4) along the *c* axis to a pseudo-tetrahedral site, although this effort may have a larger effect on BVS of the apical oxygen [56,69]. The overbonding of the apical oxygen due to cation displacement however would in turn prohibit further movement of the cation off the center, which might explain the observed low displacement and hence low BVS of the TBP cation. This temperature-dependent cation disorder can be dynamic between two pseudo-tetrahedral sites or static with the cation trapped in one of the two positions [56,69].

Serious underbonding also occurs for Ca in $CaAl_{12}O_{19}$ (BVS 1.49), but it becomes normal when Ca is replaced with larger cations such as Sr (BVS 2.03) or Pb (BVS 1.97) [69]. Substitution of Al with larger cations like Ti, Sn, Ni, Fe and Mn however aggravates the underbonding situation of Ca as cell volume increases [56]. As shown in Table 6, the BVS of Ca becomes only 1.33 for $CaAl_{10}SnMnO_{19}$. The cuboctahedron of closest-packed oxygens is too large for Ca and the size mismatch results in a “rattling” motion of Ca inside the cage, especially at elevated temperatures [14]. This unusual thermal motion is presumably responsible for the observed large thermal displacement parameters of Ca in $CaAl_{12}O_{19}$-based solid solutions [56]. The Ca U_{iso} is even bigger (0.035 Å^2) in $CaAl_{10}SnMnO_{19}$ with larger cell volume (Table 5),

notice the U_{iso} of the tetrahedral cation (Al3 site) is 0.066 Å^2, indicating a worse situation for Al3 and Mn3. As a matter of fact, it is a common feature for tetrahedral cations to be severely underbonded as well in the hibonite structure [69].

As we mentioned before, there are three crystallographically distinct octahedral sites (Al1, Al4, Al5), one tetrahedral site (Al3) and one trigonal bipyramidal site (Al2) in the hibonite structure (Fig.1). The substituted Fe^{3+} cations are distributed over all five Al sites in $CaAl_{9.5}Fe_{2.5}O_{19}$ (Table 3), with a slight preference for the tetrahedral site (Al3 site) within the spinel block (Fig.1). About 44% of total amount of incorporated Fe^{3+} enters the tetrahedral site (Al3) and the pseudo-tetrahedral or TBP site (Al2), and 56% enters the rest of the three octahedral sites (Al1, Al4, Al5). The amount of Fe at combined octahedral sites is larger simply because the multiplicity of the Al5 site is three times greater than those of the Al2 and Al3 sites. The inclination of trivalent Fe towards tetrahedral coordination has been observed in similar hibonite systems [16,23] although Fe^{3+} with a d^5 high spin configuration has no crystal field stabilization energy. The trivalent Al^{3+} on the other hand prefers high symmetry octahedral sites (Al1, Al4 and Al5) due to its higher ionic character than Fe^{3+} [71]. Fig.19(a) shows the expected increase of average M3–O (*M* = Al, Fe) bond distance in $CaAl_{12-x}Fe_xO_{19}$ with increasing *x* (*x* = 6 from [16] plotted for comparison). The average tetrahedral bond angle deviates slightly from the ideal 109.5° upon Fe substitution (Fig.19(b)). Additionally the average M4–O and M2–O (*M* = Al, Fe) distances increase by 0.024 Å and 0.047 Å (at *x* = 2.5), respectively, with Fe substitution, consistent with significant amount of Fe^{3+} entering the Al4 and Al2 sites. The M4–M4 interatomic distance also increases from 2.593 to 2.677 Å as Fe enters the face-sharing octahedral dimer, which can be attributed to the increased cation-cation repulsion. This is apparently not the case for Ni-containing hibontie solid solutions where the Al4 site is exclusively occupied by tetravalent Ti or populated by trivial amount of Ni^{2+} in the absence of Ti^{4+} [56]. The smaller and subtle change in average bond distances of M5–O and M1–O also agrees well with the rest of Fe distribution. The refined formula $CaAl_{9.47}Fe_{2.53}O_{19}$ is in good agreement with the nominal composition.

Crystal structures of $CaAl_{12-x}Mn_xO_{19}$ compositions have never been reported. Due to the low solubility of trivalent Mn^{3+} in hibonite host lattice it is very challenging to prepare single-phase $CaAl_{12-x}Mn_xO_{19}$ especially at high Mn concentration. Neutron sample with a nominal composition $CaAl_{11.5}Mn_{0.5}O_{19}$ is refined to be $CaAl_{11.62}Mn_{0.38}O_{19}$ indicating a substitution level lower than expected (Table 4). The impurity phases are determined to be $CaAl_4O_7$ and $MnAl_2O_4$ (~9%). The incorporated small amounts of Mn^{3+} substitute on all three octahedral sites and one tetrahedral site with a combined occupancy in favor of octahedral coordination. This would be expected based on the crystal field stabilization energy of Mn^{3+} (d^4) in octahedral environment [72]. Among 77% of the total amount of Mn^{3+} that enters the octahedral sites, about 50% goes to the edge-sharing octahedra (Al5). Each octahedron based on Al5 shares four of its edges with other Al5 octahedra forming a rather rigid two dimensional layer, which causes any expansion to be mainly perpendicular to the *c* axis. Although the change in bond distances is minimum, the M4–M4 (*M* = Al, Mn^{3+}) interatomic distance across the face increases by ~0.01 Å (Table 6), giving rise to a slight increase in cell edge *c* and cell volume (Fig. 14). Similar cation distribution of trivalent Mn, especially the lack of Mn^{3+} on TBP site, was found for magnetoplumbite-like $BaFe_{12-x}Mn_xO_{12}$ hexagonal ferrites [19,20].

To differentiate the scattering power contribution of Sn^{4+} and Mn^{2+} at a given Al site, neutron diffraction is more favorable due to the negative scattering length of Mn. For $CaAl_{10}SnMnO_{19}$ phase, if the scattering power of a given Al site decreases it must be due to Mn substitution, while an increase in scattering power at that site would be caused by Sn substitution. The refinement results of $CaAl_{10}SnMnO_{19}$ phase are somewhat comparable to those of $CaAl_{10}TiNiO_{19}$ [56,69]. The divalent Mn^{2+} and tetravalent Sn^{4+} show strong preference for tetrahedral (Al3) and face-sharing octahedral (Al4) sites (Table 5), respectively, just like Ni^{2+} and Ti^{4+} in $CaAl_{10}TiNiO_{19}$ blue hibonite. In addition, small amount of Mn^{2+} enters Al1 and Al2 sites and some Sn^{4+} enters the Al5 site, which is not the case for $CaAl_{10}TiNiO_{19}$. The Shannon ionic radii of Mn^{2+} are 0.75 Å for CN = 5 and 0.83 Å for CN = 6, much larger than those of Sn^{4+}, Ni^{2+} and Ti^{4+}. Due to the rigidity of the edge-sharing octahedral layer it is reasonable that Mn^{2+} favors the more flexible Al2 site over the Al5 site. And indeed the average bond distance of M2–O (*M* = Al, Mn, Sn) increases by 0.04 Å with Mn/Sn co-substitution and it is 0.013 Å larger than that in $CaAl_{10}TiNiO_{19}$. TBP coordination is well established for Ti^{4+} but not for Sn^{4+}. Instead of entering the Al2 site like Ti, some Sn^{4+} cations occupy the Al5 site like Ni^{2+}, resulting in a slight increase of the average M5–O distance. The average M4–O bond distance increases by 0.062 Å and the M4–M4 distance increases from 2.60 to 2.77, due to the much greater Sn substitution at the Al4 site (Table 6). The M4–M4 repulsion in the face-sharing octahedra gives rise to the evident expansion in cell c and cell volume through the O3–M4–O3–M4–O3 face share units (Fig.15). The enormous increase in average M3–O distance, about 0.084 Å, can be attributed to the unusually large size of Mn^{2+} (Fig.19). The tendency of Mn^{2+} to occupy the tetrahedral site within the spine1 block was also found in some lanthanum hexaaluminates with magnetoplumbite structure [46,47]. And a similar occupational hierarchy of Sn^{4+} was discovered for $BaFe_{12-x}Co_xSn_xO_{19}$ compounds through single crystal XRD study [73]. In both structures Sn^{4+} has a preference to enter face-sharing octahedral sites (Al4) and in less degree edge-sharing octahedral sites (Al5) but never the trigonal-antiprism sites (Al1).

*4.3 Optical properties: L*a*b* and UV-Vis/NIR reflectance*

Colors can be described and quantified using the CIE L*a*b* color space. It is a three dimensional color model where L^* represents a black (L^*=0)/white (L^*=100) component of color, a^* is responsible for a red (a^*>0)/green (a^*<0) component and b^* represents a yellow (b^*>0)/blue (b^*<0) component. A unique color can be defined precisely by a set of these three color coordinates. Measured $L^*a^*b^*$ values together with the recorded colors are given in Table 7 for about 71 compositions. Evidently, a wide range of colors can be designed by tuning the hibonite structure through various cation substitutions. The compositions with blue colors have been reported separately [56].

UV-Vis diffuse reflectance spectra were recorded for four solid solutions: $CaAl_{12-x}Fe_xO_{19}$ (x = 0.5–3.0), $CaAl_{12-x}Mn_xO_{19}$ (x = 0.1–0.6), $CaAl_{12-2x}Sn_xMn_xO_{19}$ (x = 0.1–1.0) and $CaAl_{12-x}Cr_xO_{19}$ (x = 0.5–3.5). As shown in Figs. 20-21, the measured reflectance has been transformed to absorbance using the Kubelka-Munk equation. Diffuse reflectance spectra of $CaAl_{10}Fe_2O_{19}$, $CaAl_{11.5}Mn_{0.5}O_{19}$, $CaAl_{10}SnMnO_{19}$ and $CaAl_{10}Cr_2O_{19}$ are plotted with respect to photon energy (eV) instead of wavelength (nm) in Fig. 21. Manifestly two to three absorption peaks are

detected in nearly all spectra across the visible range with a strong absorption centered around 2.5–3.0 eV in the blue-violet region. The second absorption peak near the yellow region of the visible spectrum looks more like a shoulder in most of the spectra except for the Cr-containing samples. The $CaAl_{12-x}Cr_xO_{19}$ solid solution exhibits two conspicuous bands (~2.12eV and ~3.12eV) known as $t^3_{2g} \rightarrow t^2_{2g}e^1_g$ transition due to electron-electron repulsion for Cr^{3+} octahedral complexes [74]. The absence of absorption in the ~2.5 eV (green) region of the spectrum brings about the green hue of the resulting olive powder (Fig.21 and Table 7). For solid solutions without Cr, relatively strong absorption in the blue-cyan region combined with weak absorption in the red region may account for the observed brown color with reddish or orange hue. The dullness of most samples can be ascribed to the lack of one distinct narrow absorption peak. In Fig.20 as the concentration of the chromophore ion increases, the lower-energy absorption peak broadens and the higher-energy onset shifts to lower energy, consistent with the gradual darkening of the samples with *x*. We assign the lower-energy absorption to d-d transition and the higher-energy peak to the O 2p to metal 3d charge transfer. The actual situation could be very complicated as a consequence of the chromophore ions occupying multiple sites with various coordination numbers in the hibonite host structure.

High reflectance in the near infrared (NIR) region is an essential property of "Cool pigments", i.e. pigments that reflect heat and stay cool under sun light. NIR reflectance spectra of $CaAl_{12-x}Fe_xO_{19}$ (x = 0.5–3.0), $CaAl_{12-x}Mn_xO_{19}$ (x = 0.1–0.6), $CaAl_{12-2x}Sn_xMn_xO_{19}$ (x = 0.1–1.0) and $CaAl_{12-x}Cr_xO_{19}$ (x = 0.5–3.5) solid solutions measured in the range of 700–2500 nm are demonstrated in Fig. 22 together with the spectrum of commercial Co-blue. Unlike the spectra of Ni-containing blue hibonites, no strange three-peak-valley feature is observed in these samples [56]. Although the total NIR reflectance decreases with *x*, all synthesized compounds show relatively high reflectance (70–80%) in NIR region, better than the commercial Co-blue (Fig. 22(a)). Our colored hibonite oxides are therefore promising candidates for cool pigment applications.

4.4 Magnetism

Magnetic measurements were performed for $CaAl_{11.5}Mn_{0.5}O_{19}$ and $CaAl_{11}Ti_{0.5}Mn_{0.5}O_{19}$ samples to verify the oxidation states of manganese ions. Temperature dependence of magnetic susceptibility (χ) is given in Fig. 23. Using the slope and intercept of the linear region of inverse magnetic susceptibility ($1/\chi$) vs. temperature plots (Fig. 23), Curie constants (C) and Weiss constants (θ_W) are determined. Effective magnetic moments (μ_{eff}) are calculated (Table 8) from Curie constants with diamagnetic correction [65]. The studied compounds show paramagnetic behavior in the measured temperature range 5–300 K. There is a small shoulder around 40K on the χ and $1/\chi$ vs. temperature curves of the $CaAl_{11.5}Mn_{0.5}O_{19}$ phase. We believe that spinel $MnAl_2O_4$, the impurity phase in $CaAl_{11.5}Mn_{0.5}O_{19}$ sample, is responsible for this abnormal feature, since it undergoes a magnetic phase transition at the same temperature [75].

The calculated effective magnetic moment values are comparable to the theoretical spin-only magnetic moments for high spin Mn^{3+} ($3d^4$, μ_{th} = 4.89 μ_B) in $CaAl_{11.5}Mn_{0.5}O_{19}$ and Mn^{2+} ($3d^5$, μ_{th} = 5.92 μ_B) in $CaAl_{11}Ti_{0.5}Mn_{0.5}O_{19}$. The existence of trivalent Mn^{3+} and divalent Mn^{2+} in

these two hibonite phases is confirmed experimentally. Similarly, divalent Mn^{2+} in $CaAl_{10}SnMnO_{19}$ is expected.

4.5 Dielectric properties

Dielectric properties of hibonite materials are not well studied. Arora A. and coauthors [76] investigated the dielectric properties of co-substituted *M*-type barium hexaferrites, compounds that are isostructural to hibonite. Recently we reported dielectric data of $CaAl_{11}Ti_{0.5}Ni_{0.5}O_{19}$ and $CaAl_{10}TiNiO_{19}$ hibonite-type oxides with bright blue colors [56].

In this work, dielectric measurements were carried out for $CaAl_{11.5}Fe_{0.5}O_{19}$ and $CaAl_{11.4}Sn_{0.3}Mn_{0.3}O_{19}$ phases at frequencies of 1, 10, 100, 500, 750 kHz and 1 MHz and in the temperature range 25–250°C. Dielectric constant (κ) and dielectric loss (δ) (at varied frequencies) as a function of temperature are shown in Fig. 24. Frequency dependence of dielectric constant and dielectric loss of $CaAl_{11.5}Fe_{0.5}O_{19}$ and $CaAl_{11.4}Sn_{0.3}Mn_{0.3}O_{19}$ at room temperature are given in Fig. 25.

Theoretical values of dielectric constants (κ_{th}) are calculated according to Subramanian et al. [77]: κ_{th} = 9.37 for $CaAl_{11.5}Fe_{0.5}O_{19}$ and κ_{th} = 9.42 for $CaAl_{11.4}Sn_{0.3}Mn_{0.3}O_{19}$. Compared with the estimated κ_{th} values, $CaAl_{11.5}Fe_{0.5}O_{19}$ phase shows smaller experimental κ, and the experimental κ values of $CaAl_{11.4}Sn_{0.3}Mn_{0.3}O_{19}$ phase are smaller than the theoretical κ_{th} at all frequencies except for 1 MHz. In the case of $CaAl_{11.5}Fe_{0.5}O_{19}$, the rather consistent dielectric constant and dielectric loss experience a strong temperature dependency at 1 and 10 kHz (100 kHz for dielectric loss only) below 50°C and an abrupt increase in dielectric loss at 1 kHz above 150°C. The dielectric constant and loss of $CaAl_{11.4}Sn_{0.3}Mn_{0.3}O_{19}$ phase, on the other hand, are frequency-dependent only and fairly constant over the entire temperature range of measurement at a given frequency.

5. Conclusions

We demonstrate in the present work that various colors can be induced in hibonite host $CaAl_{12}O_{19}$ by tuning the crystal structure through *M*-site substitution using standard solid state synthesis method. Majority of our $CaAl_{12-x}M_xO_{19}$ phases are reported for the first time. The crystal structures of $CaAl_{9.5}Fe_{2.5}O_{19}$, $CaAl_{11.5}Mn_{0.5}O_{19}$ and $CaAl_{10}SnMnO_{19}$ are refined using neutron powder diffraction data. Optical properties of all the samples are characterized using *L*a*b** color space and diffuse reflectance measurements. Magnetic measurements proved the existence of Mn^{3+} and Mn^{2+} in $CaAl_{11.5}Mn_{0.5}O_{19}$ and $CaAl_{11}Ti_{0.5}Mn_{0.5}O_{19}$ accordingly. Synthesized color compounds are cheap, durable, mostly nontoxic and promising candidates for cool pigments application due to their relatively high reflectance in the NIR region.

Acknowledgments

This research was supported by National Science Foundation (DMR-1508527). We thank Judith K. Stalick for neutron data collection and the fruitful collaboration. The identification of any commercial product or trade name does not imply endorsement or recommendation by the National Institute of Standards and Technology.

References

[1] Townes WD, Fang JH, Perrotta AJ. The crystal structure and refinement of ferrimagnetic barium ferrite, $BaFe_{12}O_{19}$. Z Kristallogr 1967;125:437-49.

[2] Aleshko-Ozhevskii OP, Faek MK, Yamzin II. A neutron diffraction study of the structure of magnetoplumbite. Sov Phys Crystallogr 1969;14(3):367-9.

[3] Grey IE, Madsen IC, Haggerty SE. Structure of a new upper-mantle, magnetoplumbite-type phase, $Ba[Ti_3Cr_4Fe_4Mg]O_{19}$. Am Mineral 1987;72:633-6.

[4] Bermanec V, Sturman D, Criddle AJ, et al. Nezilovite, a new member of the magnetoplumbite group, and the crystal chemistry of magnetoplumbite and hibonite. Can Mineral 1996;34:1287-97.

[5] Keil K, Fuchs LH. Hibonite [$Ca_2(Al,Ti)_{24}O_{38}$] from the leoville and allende chondritic meteorites. Earth Planet Sci Lett 1971;12:184-90.

[6] Kahl A, Lejus AM, Madsac M, Thery J, Vivien D. Preparation, structure, optical, and magnetic properties of lanthanide aluminate single crystals ($LnMAl_{11}O_{19}$). J Appl Phys 1981;52(11):6864-9.

[7] Li YJ, Ma YY, Ye S, Hu GP, Zhang QY. Site-related near-infrared luminescence in $MAl_{12}O_{19}$ (M = Ca, Sr, Ba): Fe^{3+} phosphors. Mater Res Bull 2014;51:1-5.

[8] Collongues R, Gourier D, Kahn-Harari A, et al. Magnetoplumbite-related oxides. Annu. Rev Mater Sci 1990;20:51-82.

[9] Bergstein A, White WD. Manganese-activated luminescence in $SrAl_{12}O_{19}$ and $CaAl_{12}O_{19}$. J Electrochem Soc 1971;118(7):1166-71.

[10] Verstegen JMPJ, Sommerdijk JL, Verriet JG. Cerium and terbium luminescence in $LaMgAl_{11}O_{19}$. J Lumin 1973;6:425-31.

[11] Curien H, Guillemin C, Orcel J, et al. La hibonite, nouvelle espese minerale. Comptes Rendus de l'Academie des Sciences, Paris 1956:2845-7.

[12] Utsunomiya A, Tanaka K, Morikawa H, Marumo F, Kojima H. Structure refinement of $CaO{\bullet}6Al_2O_3$. J Solid State Chem 1988;75:197-200.

[13] Wagner TR, O'Keeffe M. Bond lengths and valences in aluminates with the magnetoplumbite and β-alumina structures. J Solid State Chem 1988;73(1):211-6.

[14] Nagashima M, Armbruster T, Hainschwang T. A temperature-dependent structure study of gem-quality hibonite from Myanmar. Mineral Mag 2010;74:871-85.

[15] Kohn JA, Eckart DW. New hexagonal ferrite, establishing a second structural series. J Appl Phys 1964;35:968-70.

[16] Harder M, Muller-Buschbaum H. $CaFe_6Al_6O_{19}$ mit magnetoplumbitstruktur. Z Naturforsch B Chem Sci 1977;32(7):833-4 (in German).

[17] Pausch H, Mueller-Buschbaum H. Zur metallverteilung in $SrFe_7Al_5O_{19}$. Z Naturforsch B Chem Sci 1976;31(8):1148 (in German).

[18] Kimura K, Ohgaki M, Tanaka K, et al. Study of the bipyramidal site in magnetoplumbite-like compounds, $SrM_{12}O_{19}$ (M = Al, Fe, Ga). J Solid State Chem 1990;87:186-94.

[19] Collomb A, Obradors X, Isalgue A, Fruchart D. Neutron diffraction study of the crystallographic and magnetic structures of the $BaFe_{12-x}Mn_xO_{19}$ m-type hexagonal ferrites. J Magn Magn Mater 1987;69(3):317-24.

[20] Jirak DZ, Krupka M, Pollert E. Cation distribution in hexaferrites $BaFe_{12-x}Mn_xO_{19}$. Cryst Res Technol 1987;22(4):K71-3.

[21] Ounnunkad S, Phanichphant S, Winotai P, Tang I-M. Cr-site preference of $BaFe_{12-x}Cr_xO_{19}$ hexaferrite ceramics monitored by Mossbauer spectroscopy. Phys Stat Sol (b) 2007;244(6):2190-8.
[22] Okube M, Yoshizaki J, Toyoda T, Sasaki S. Cation distribution and magnetic structure of *M*-type $BaTiMnFe_{10}O_{19}$ examined by synchrotron X-ray and neutron studies. J Appl Cryst 2016;49:1433.
[23] Sandiumenge F, Gali S, Rodriguez J. X-ray profile analysis of cation distribution in $SrAl_xFe_{12-x}O_{19}$ solid solution. Mat Res Bull 1988;23:685-92.
[24] Prakash CS, Kulkami DK. Chromium substituted hexagonal calcium ferrites. Indian J Pure Appl Phys 1994;32:361-3.
[25] Mamatha C, Krishnaiah M, Prakash CS, Rewetkar KG. Structural and electrical properties of aluminium substituted nano calcium ferrites. Procedia Mat Sci 2014;5:780-6.
[26] Na EH, Song S, Koo Y-M, Jang HM. Relaxor-like improper ferroelectricity induced by S_i•S_j-type collinear spin ordering in a M-type hexaferrite $PbFe_6Ga_6O_{19}$. Acta Mater 2013;61:7705-11.
[27] Ahn SD, Jung HS, Choo DC, et al. White organic light-emitting devices fabricated utilizing a down-conversion $CaAl_{12}O_{19}$:Mn phosphor layer. J Electrochem Soc 2010;157(6):J238-40.
[28] Kojima H, Sugimoto M. Ferromagnetic Materials. Eds. Wolfarth EP. North-Holland, Amsterdam 1982;3:305-93.
[29] Vinnik DA, Zherebtsov DA, Mashkovtseva LS, et al. Growth, structural and magnetic characterization of Al-substituted barium hexaferrite single crystals. J Alloys Compd 2014;615:1043-46.
[30] Tronc E, Laville F, Gasperin M, Lejus AM, Vivien D. Structural and spectroscopic investigations of $LaFeAl_{11}O_{19}$ compounds. J Solid State Chem 1989;81(2):192-202.
[31] Schwanitz SU, Buschbaum HM. Neue Lanthanoidmagnetoplumbite: $LaFe_{11}AlO_{19}$, $SmFe_4Al_8O_{19}$ und $Eu_{0.83}Fe_2Al_{10}O_{19}$. Monatsh Chem 1982;113:1079-85 (in German).
[32] Ounnunkad S, Winotai P, Phanichphant S. Effect of La doping on structural, magnetic and microstructural properties of $Ba_{1-x}La_xFe_{12}O_{19}$ ceramics prepared by citrate combustion process. J Electroceram 2006;16:357-61.
[33] Luo H, Rai BK, Mishra SR, Nguyen VV, Liu JP. Physical and magnetic properties of highly aluminum doped strontium ferrite nanoparticles prepared by auto-combustion route. J Magn Magn Mater 2012;324:2602-8.
[34] Ihinger PD, Stolper E. The color of meteoritic hibonite: an indicator of oxygen fugacity. Earth Planet Sci Lett 1986;78:67-79.
[35] Burns RG. Mixed valency minerals: influences of crystal structures on optical and Moessbauer spectra. Eds. Prassides K. NATO ASI Series, Series C: Math Phys Sci 1991;343(Mixed Valency Syst: Appl Chem Phys Biol):175-99.
[36] Simon SB, Davis AM, Grossman L. Formation of orange hibonite, as inferred from some Allende inclusions. Meteorit Planet Sci 2001;36:331-50.
[37] Hainschwang T, Notari F, Massi L, Armbruster T, Rondeau B, Fritsch E, Nagashima M. Hibonite: a new gem mineral. Gems Gemol 2010;46(2):135-8.
[38] Dyar MD, Solberg TC, Burns RG. The effects of composition, oxygen fugacity, and crystal structure on the color of hibonite (abstr.). Lunar Planet Sci XVII 1986:194-5.
[39] Armstrong JT, Meeker GP, Huneke JC, Wasserburg GJ. The Blue Angel: I. The mineralogy and petrogenesis of a hibonite inclusion from the Murchison meteorite. Geochimica et Cosmochimica Acta 1982;46:575-95.

[40] Burns RG, Burns VM. Crystal chemistry of meteoritic hibonites. J Geophys Res 1984;89:C313-21.
[41] Ma C. Hibonite-(Fe), (Fe,Mg)$Al_{12}O_{19}$, a new alteration mineral from the Allende meteorite, Am Mineral 2010;95:188-91.
[42] Holtsman D. Iron in hibonite: A spectroscopic study. Phys Chem Miner 1996;23(7):452-60.
[43] Saber D, Lejus AM. Elaboration and characterization of lanthanide aluminate single crystals with the formula $LnMgAl_{11}O_{19}$. Mat Res Bull 1981;16:1325-30.
[44] Doyle PM, Schofield PF, Berry AJ, et al. Substitution of Ti^{3+} and Ti^{4+} in hibonite ($CaAl_{12}O_{19}$). Am Mineral 2014;99:1369-82.
[45] Rout SS, Bischoff A. Chemical composition of Ca,Al-rich inclusions in Rumuruti (R) chondrites. Meteorit Planet Sci 2008;43(7):A134.
[46] Gasperin M, Saine MC, Kahn A, et al. Influence of M^{2+} ions substitution on the structure of lanthanum hexaaluminates with magnetoplumbite structure. J Solid State Chem 1984;54:61-9.
[47] Laville F, Lejus AM. Crystal growth and characterization of $LaMO_{11}O_{19}$ lanthanum aluminates. J Cryst Growth 1983;63:426-8.
[48] Gourier D, Laville F, Vivien D. X-ray induced defects and thermoluminescent properties of lanthanum hexaaluminates with magnetoplumbite-like structure. J Solid State Chem 1986;61:67-80.
[49] Graetsch H, Gebert W. Short Cr^{3+}-Cr^{3+} distances in magnetoplumbite type $SrCr_6Ga_3O_{19}$. Z Kristallogr 1996;211:25-30.
[50] Ardit M, Borcanescu S, Cruciani G, et al. Ni-Ti codoped hibonite ceramic pigments by combustion synthesis: crystal structure and optical properties. J Am Ceram Soc 2016;99:1749-60.
[51] Costa G, Ribeiro MJ, Hajjaji W, et al. Ni-doped hibonite ($CaAl_{12}O_{19}$): A new turquoise blue ceramic pigment. J Eur Ceram Soc 2009;29:2671-8.
[52] Kim G, Lee B-H. Synthesis and mechanism of Ni-doped hibonite blue pigments. Kor J Mater Res 2014;24(1):43-7 (in Korean).
[53] Leite A, Costa G, Hajjaji W, et al. Blue cobalt doped-hibonite pigments prepared from industrial sludges: formulation and characterization. Dyes Pigm 2009;81:211-7.
[54] Hajjaji W, Costa G, Zanelli C, et al. An overview of using solid wastes for pigments industry. J Eur Ceram Soc 2012;32:753-65.
[55] Hajjaji W, Seabra MP, Labrincha JA. Recycling of solid wastes in the systhesis of Co-bearing calcium hexaluminate pigment. Dyes Pigm 2009;83:385-90.
[56] Li J, Medina EA, Stalick JK, Sleight AW, Subramanian MA. Colored oxides with hibonite structure: A potential route to non-cobalt blue pigments. Prog Solid State Chem 2016:1-16.
[57] Subramanian MA, Li J, Sleight AW. Compounds comprising a hibonite structure. UC Patent;WO2015131036:A120150903,2015.
[58] Haberey F, Leckebusch R, Rosenberg M, Sahl K. Flux growth of $SrGa_{12}O_{19}$ single crystals. J Cryst Growth 1983;61:284-8.
[59] Mateika D, Laudan M. Czochralski growth of barium hexaaluminate single-crystals. J Cryst Growth 1979;46(1):85-90.
[60] Vivien D, Lejus AM, Thery J, Collongues R, Aubert JJ, et al. Observation of the continuous laser effect in $La_{0.9}Nd_{0.1}MgAl_{11}O_{19}$ aluminate single-crystals (LNA) grown by the Czochralski method. C. R. Acad. Sci. Paris (II) 1984;298(6)195-8.
[61] Larson AC, Von Dreele RB. General Structure Analysis System (GSAS); Report LAUR 86-748; Los Alamos National Laboratory, Los Alamos, NM 1994.

[62] EXPGUI, a graphical user interface for GSAS: Toby BH. J Appl Crystallogr 2001:34:210.
[63] Hormillosa C, Healy S, Stephen T, Brown ID. Bond Valence Calculator, Version 2.0 (1993) http://www.ccp14.ac.uk (accessed 09.09.2016).
[64] Sherif ME, Bayoumi OA, Sokkar TZN. Prediction of absorbance from reflectance for an absorbing-scattering fabric. Color Res Appl 1997;22(1):32-9.
[65] Bain GA, Berry JF. Diamagnetic corrections and Pascal's constants. J Chem Educ 2008;85:532-6.
[66] Gawali SR, Rewatkar KG, Nanoti VM. Structural and electrical properties of M-type nanocrystalline aluminium substituted calcium hexaferrites. Adv Appl Sci Res 2012;3(5):2672-8.
[67] Shannon RD. Revised effective ionic radii and systematic studies of interatomic distances in halides and chalcogenides. Acta Cryst 1976;A32:751-67.
[68] https://www.ncnr.nist.gov/resources/n-lengths/elements/mn.html (accessed 09.09.2016).
[69] Li J, Medina EA, Stalick JK, Sleight AW, Subramanian MA. Structural studies of $CaAl_{12}O_{19}$, $SrAl_{12}O_{19}$, $La_{2/3+\delta}Al_{12-\delta}O_{19}$, and $CaAl_{10}NiTiO_{19}$ with the hibonite structure; indications of an unusual type of ferroelectricity. Z Naturforsch B Chem Sci 2016;71(5):475-84.
[70] Giannini M. The crystal chemistry of hibonite: an indicator for oxygen fugacity during Solar nebula condensation? Doctoral dissertation, 2014.
[71] Bertaut EF, Deschamps A, Pauthenet R. Substitution dans les hexaferrites de lion Fe^{3+} par Al^{3+}, Ga^{3+}, Cr^{3+}. J Phys Rad 1959;20:404-8.
[72] Dunitz JD, Orgel LE. Stereochemistry of ionic solids. Adv Inorg Radiochem 1960;2:1-60.
[73] Sandiumenge F, Martinez B, Batlle X. Cation distribution and magnetization of $BaFe_{12-2x}Co_xSn_xO_{19}$ (x = 0.9, 1.28) single crystals. J Appl Phys 1992;72(10):4608-14.
[74] Atkins PW. Shriver&Atkins' Inorganic Chemistry, 5th ed., Freeman WH and Company, New York, 2010:487-504.
[75] Harikrishnan SN, Zhendong F, Jorg V, Yixi S, Bruckel T. Approaching the true ground state of frustrated *A*-site spinels: A combined magnetization and polarized neutron scattering study. Phys Rev B 2014;89:174431-9
[76] Arora A, Narang SB. Structural and dielectric properties of co-substituted M-type barium hexaferrite. J Mater Sci: Mater Electron 2016;27:10157-62.
[77] M.A. Subramanian, R.D. Shannon, Dielectric constant of Y-stabilized zirconia, the polarizability of zirconia and the oxide additivity rule, Mat Res Bull 24 (1989) 1477–83.

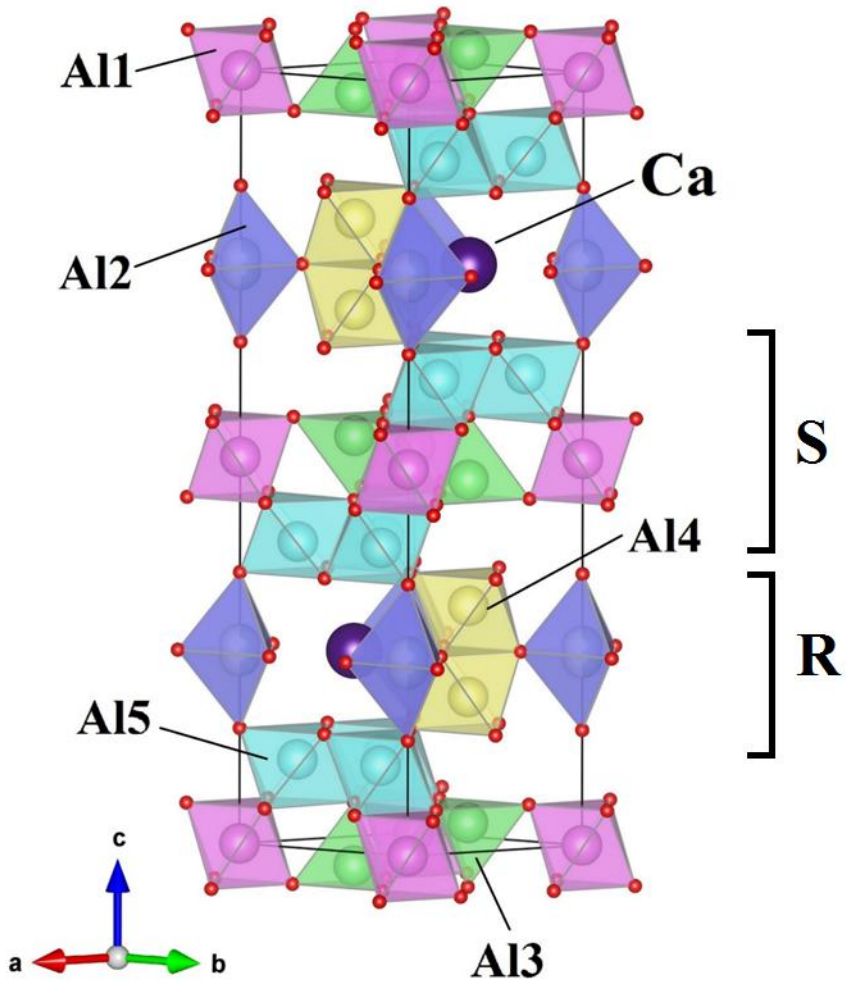

Fig. 1. Hexagonal structure of hibonite $CaAl_{12}O_{19}$ with five different crystallographic positions of aluminum: Al1: trigonal antiprismatic; Al2: trigonal bipyramidal (TBP); Al3: tetrahedral; Al4: face-sharing octahedral and Al5: edge-sharing octahedral. The crystal structure consists of two building blocks alternating along the *c*-axis: the spinel layer (S-block) and the trigonal bipyramidal layer (R-block).

Fig. 2. Colors resulted from iron substitution in the hibonite host with an ideal formula $CaAl_{12}O_{19}$: (a) $CaAl_{12-x}Fe_xO_{19}$, (b) $CaAl_{11-x}GaFe_xO_{19}$, (c) 1: $CaAl_{9.5}InSn_{0.5}Cu_{0.5}Fe_{0.5}O_{19}$, 2: $CaAl_{9.5}GaSn_{0.5}Cu_{0.5}Fe_{0.5}O_{19}$, 3: $CaAl_{9.5}InTi_{0.5}Cu_{0.5}Fe_{0.5}O_{19}$, 4: $CaAl_{9.5}GaTi_{0.5}Cu_{0.5}Fe_{0.5}O_{19}$.

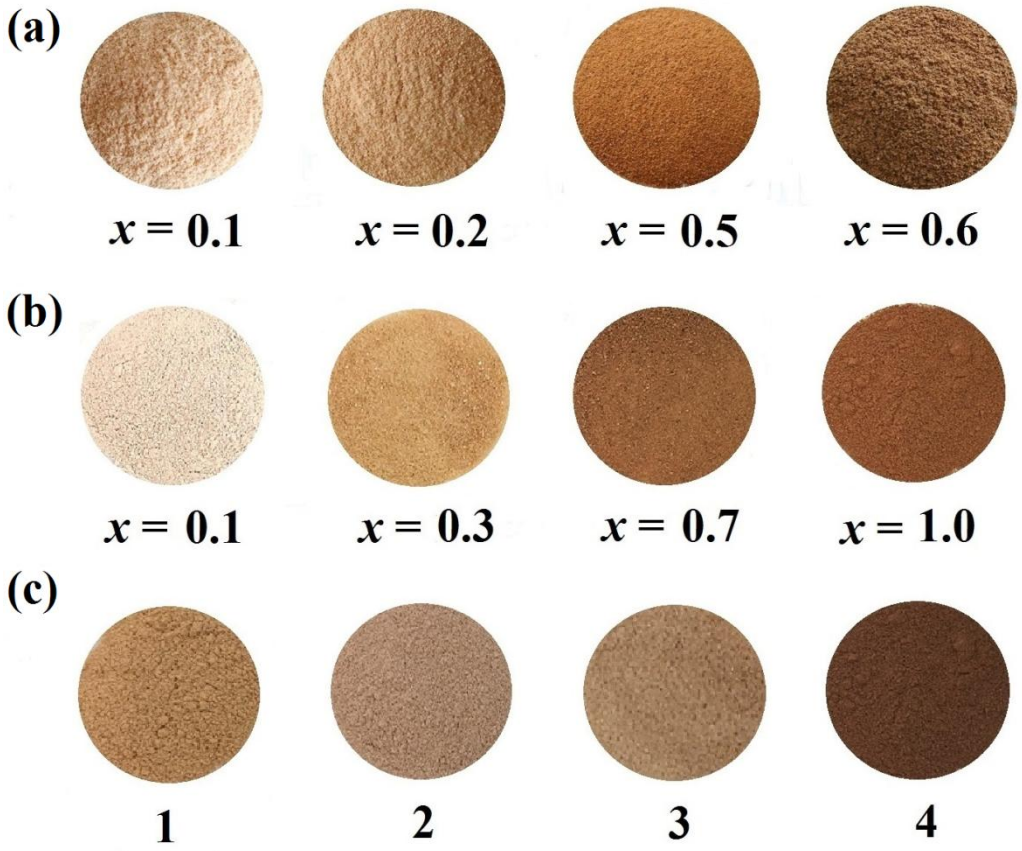

Fig. 3. Colors resulted from manganese substitution in the hibonite host with an ideal formula $CaAl_{12}O_{19}$: (a) $CaAl_{12-x}Mn_xO_{19}$, (b) $CaAl_{12-x}Sn_xMn_xO_{19}$, (c) 1: $CaAl_{10.5}Ti_{0.5}Cu_{0.5}Mn_{0.5}O_{19}$, 2: $CaAl_{10.5}Sn_{0.5}Cu_{0.5}Mn_{0.5}O_{19}$, 3: $CaAl_{9.5}InTi_{0.5}Cu_{0.5}Mn_{0.5}O_{19}$, 4: $CaAl_{9.5}InSn_{0.5}Cu_{0.5}Mn_{0.5}O_{19}$.

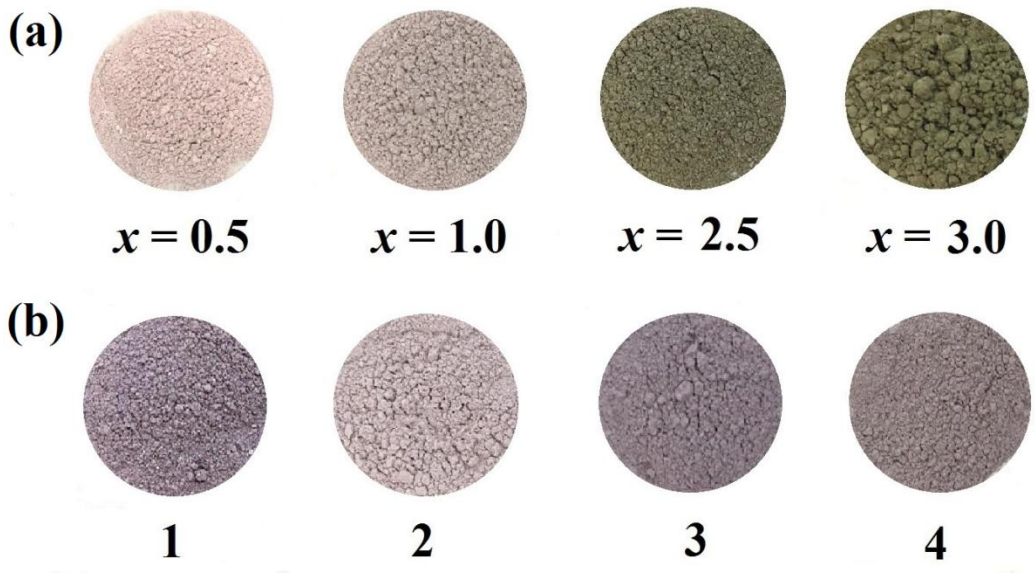

Fig. 4. Colors resulted from chromium substitution in the hibonite host with an ideal formula $CaAl_{12}O_{19}$: (a) $CaAl_{12-x}Cr_xO_{19}$, (b) 1: $CaAl_{10.5}Sn_{0.5}Cu_{0.5}Cr_{0.5}O_{19}$, 2: $CaAl_{10.5}GaCr_{0.5}O_{19}$, 3: $CaAl_{10.5}Ge_{0.5}Cu_{0.5}Cr_{0.5}O_{19}$, 4: $CaAl_{10.5}Ti_{0.5}Cu_{0.5}Cr_{0.5}O_{19}$.

Table 1 List of selected solid solutions and compositions examined by XRD.

Formula of compounds	Range of *x* or *M* cations	XRD patterns
$CaAl_{12-x}Fe_xO_{19}$	x = 0.5–4.5	Fig. 5
$CaAl_{11-x}GaFe_xO_{19}$	x = 0.5–2.5	Fig. 6(a)
$CaAl_{10}GeFeO_{19}$	–	Fig. 6(b)
$CaAl_{12-2x}Sn_xFe_xO_{19}$	x = 0.5–1.5	Fig. 6(b)
$CaAl_{12-2x}Ti_xFe_xO_{19}$	x = 0.5; 1.0	Fig. 6(b)
$CaAl_{12-x}Mn_xO_{19}$	x = 0.1–0.6	Fig. 7
$CaAl_{12-2x}Sn_xMn_xO_{19}$	x = 0.1–1.0	Fig. 8(a)
$CaAl_{10}GeMnO_{19}$	–	Fig. 8(b)
$CaAl_{12-2x}Ti_xMn_xO_{19}$	x = 0.5; 1.0	Fig. 8(b)
$CaAl_{12-x}Cr_xO_{19}$	x = 0.5–3.5	Fig. 9(a)
$CaAl_{11-x}MCr_xO_{19}$	M(III) = Ga, In; x = 0.5; 1.0	Fig. 9(b)
$CaAl_{11}M_{0.5}Cu_{0.5}O_{19}$	M(IV) = Ge, Sn	Fig. 10
$CaAl_{12-2x}Ti_xCu_xO_{19}$	x = 0.5–1.5	Fig. 10
$CaAl_{11}M'_{0.5}M''_{0.5}O_{19}$	M'(III) = Fe, Cr; M''(III) = Fe, Mn	Fig. 11(a)
$CaAl_{11-x}Ti_{0.5}Cu_{0.5}Mn_xO_{19}$	x = 0.5; 1.0	Fig. 11(b)
$CaAl_{11-x}Ti_{0.5}Cu_{0.5}M_{0.5}O_{19}$	M(III) = Fe, Cr	Fig. 11(b)
$CaAl_{10.5}Ti_{0.5}Cu_{0.5}Mn_{0.25}Fe_{0.25}O_{19}$	–	Fig. 11(b)
$CaAl_{10.5}M'_{0.5}Cu_{0.5}M''_{0.5}O_{19}$	M'(IV) = Ge, Sn; M''(III) = Fe, Mn, Cr	Fig. 11(c)
$CaAl_{10.5}Sn_{0.5}Cu_{0.5}Mn_{0.25}Fe_{0.25}O_{19}$	–	Fig. 11(c)
$CaAl_{9.5}GaM'_{0.5}Cu_{0.5}M''_{0.5}O_{19}$	M'(IV) = Ti, Sn; M''(III) = Fe, Mn, Cr	Fig. 12(a)
$CaAl_{9.5}InM'_{0.5}Cu_{0.5}M''_{0.5}O_{19}$	M'(IV) = Ti, Sn; M''(III) = Fe, Mn, Cr	Fig. 12(b)

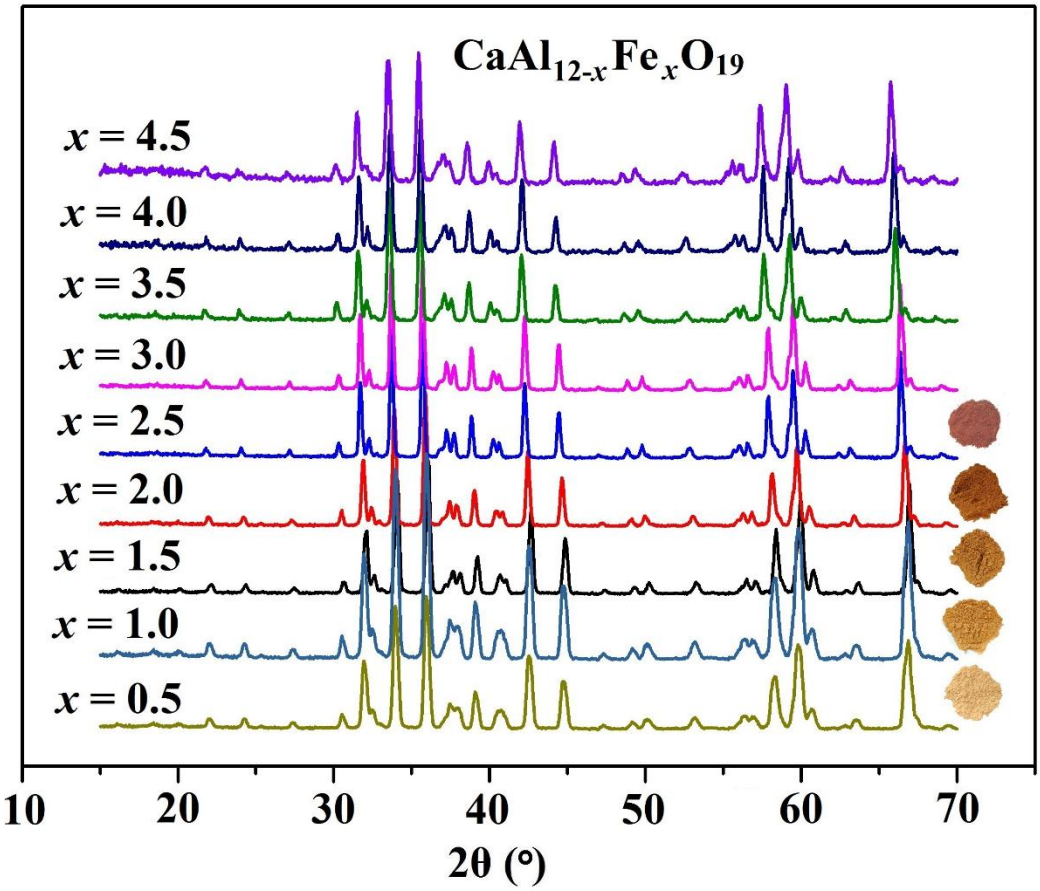

Fig. 5. XRD patterns of $CaAl_{12-x}Fe_xO_{19}$ (x = 0.5–4.5) series.

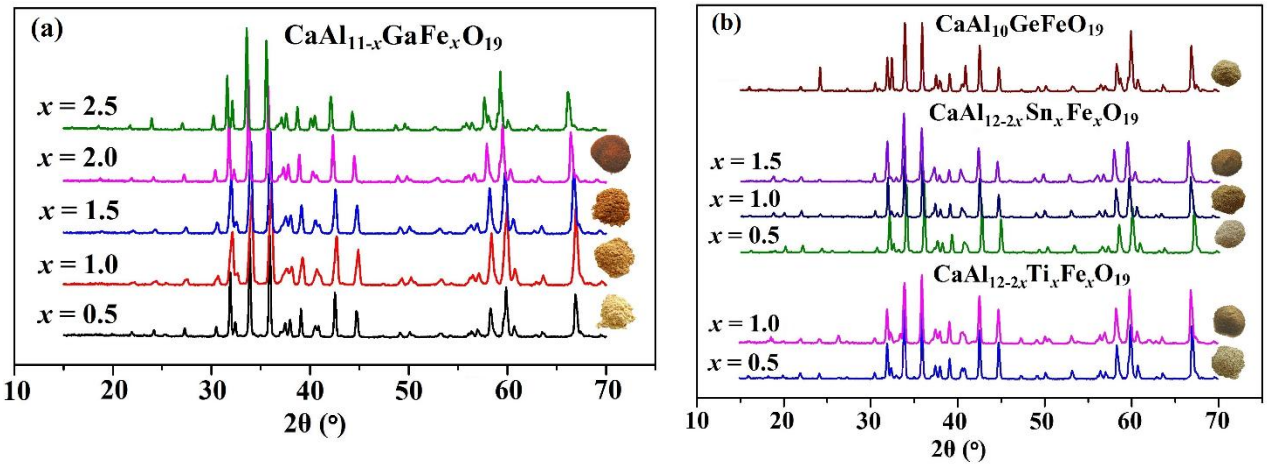

Fig. 6. XRD patterns of (a) $CaAl_{11-x}GaFe_xO_{19}$ (x = 0.5–2.5) and (b) $CaAl_{10}GeFeO_{19}$, $CaAl_{12-2x}Sn_xFe_xO_{19}$ (x = 0.5–1.5) and $CaAl_{12-2x}Ti_xFe_xO_{19}$ (x = 0.5; 1.0) solid solutions.

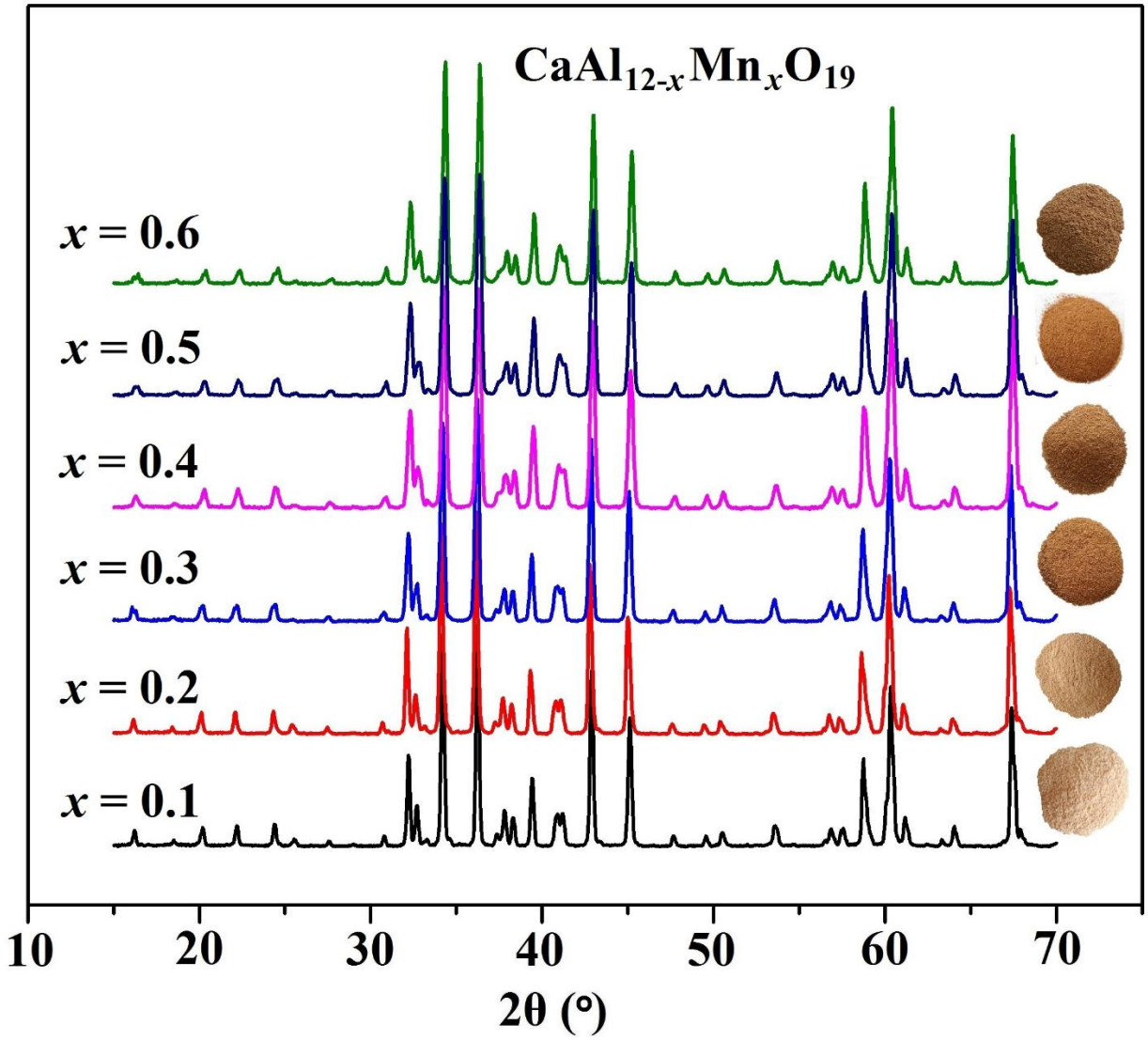

Fig. 7. XRD patterns of $CaAl_{12-x}Mn_xO_{19}$ (x = 0.1–0.6) solid solution.

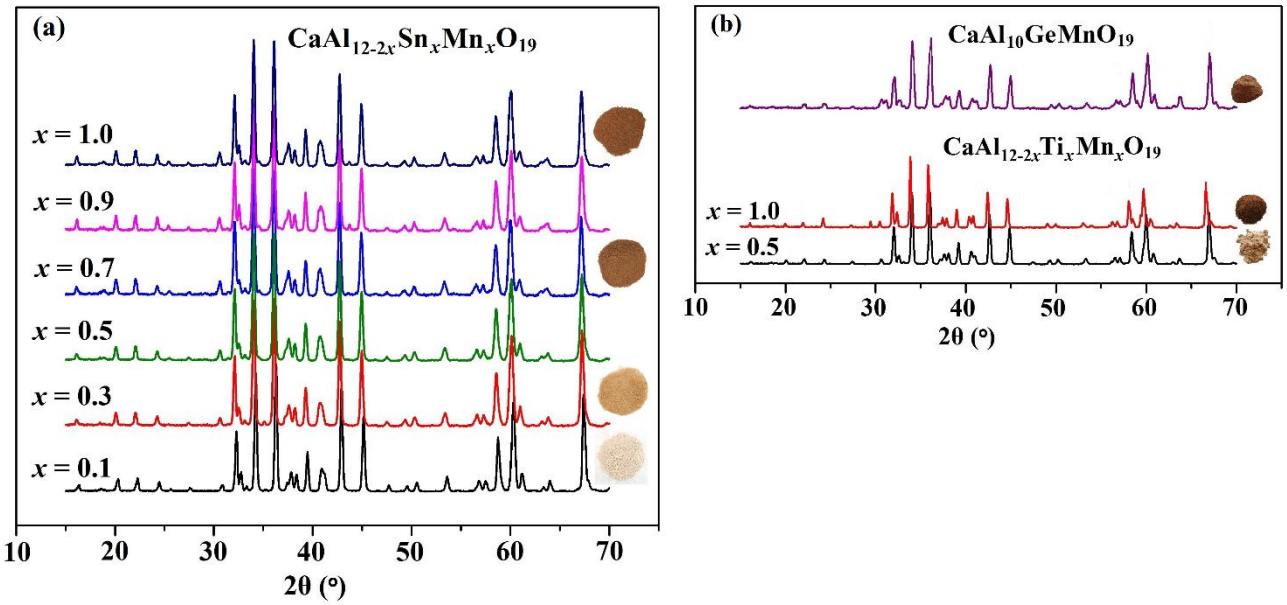

Fig. 8. XRD patterns of Mn-containing compounds: (a) $CaAl_{12-2x}Sn_xMn_xO_{19}$ (x = 0.1–1.0); (b) $CaAl_{10}GeMnO_{19}$ and $CaAl_{12-2x}Ti_xMn_xO_{19}$ (x = 0.5; 1.0).

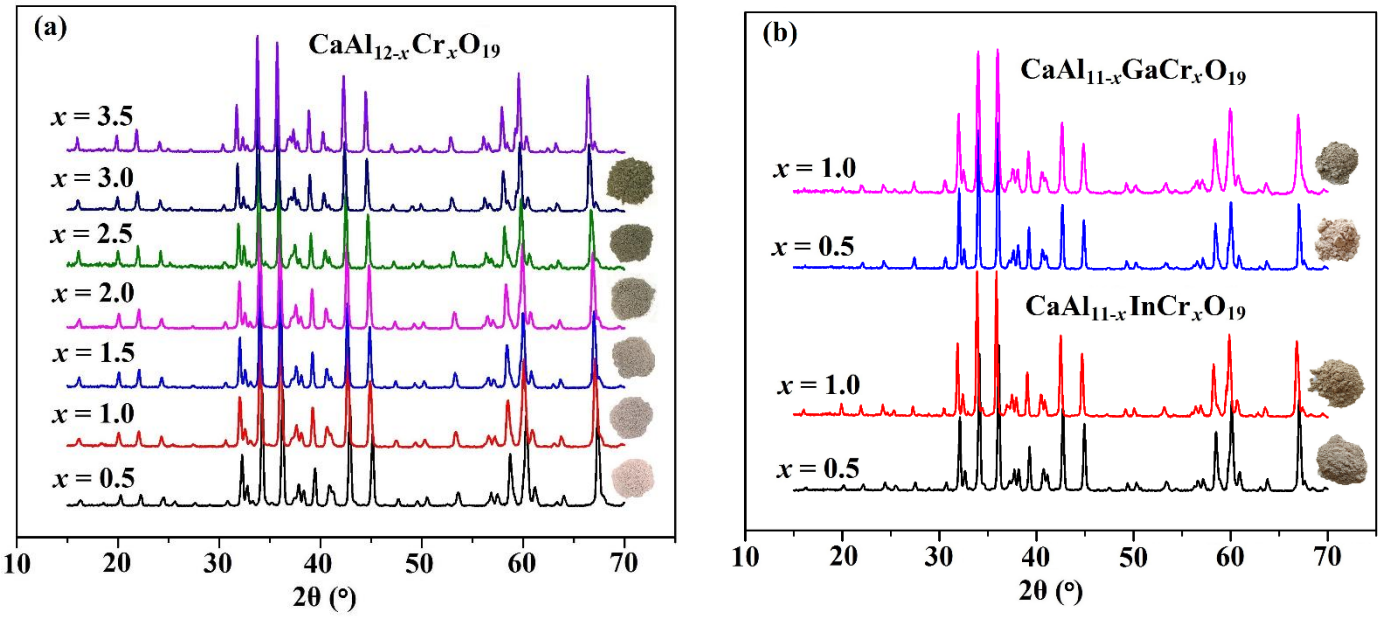

Fig. 9. XRD patterns of Cr-containing compounds: (a) $CaAl_{12-x}Cr_xO_{19}$ (x = 0.5–3.5); (b) $CaAl_{11-x}GaCr_xO_{19}$ (x = 0.5; 1.0) and $CaAl_{11-x}InCr_xO_{19}$ (x = 0.5; 1.0).

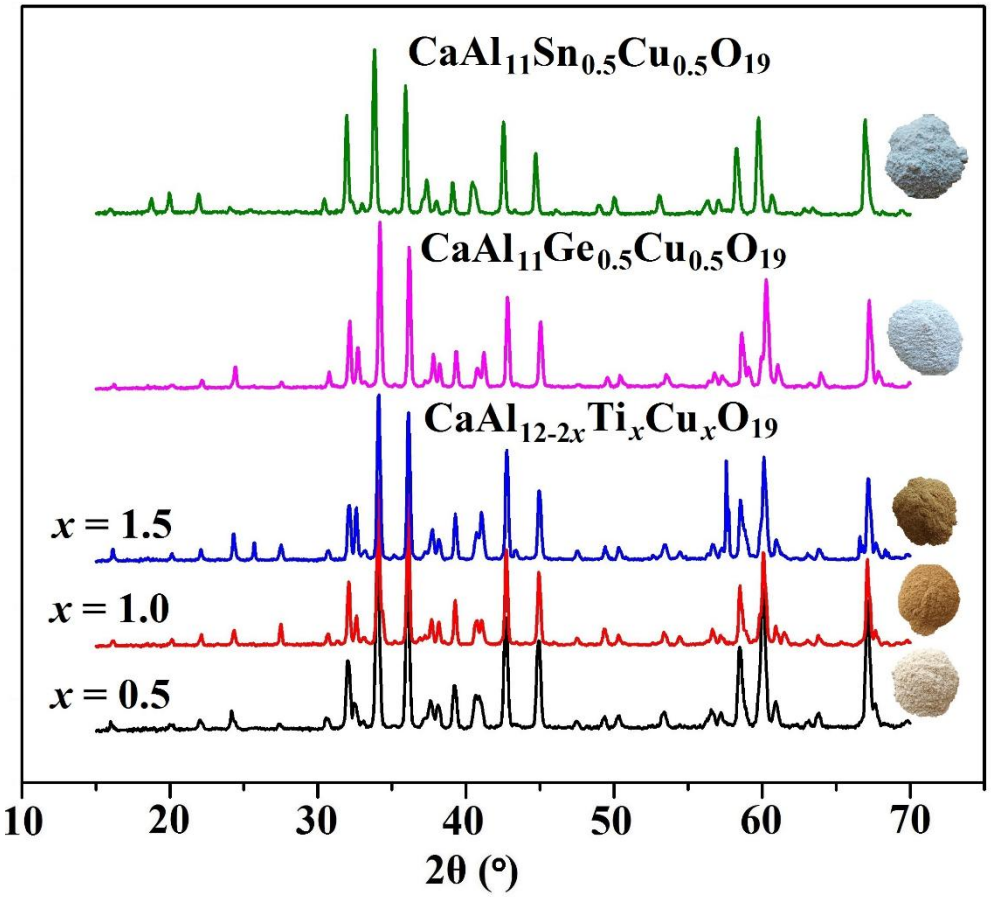

Fig. 10. XRD patterns of Cu-containing compounds: $CaAl_{11}Sn_{0.5}Cu_{0.5}O_{19}$, $CaAl_{11}Ge_{0.5}Cu_{0.5}O_{19}$ and $CaAl_{12-2x}Ti_xCu_xO_{19}$ (x = 0.5–1.5).

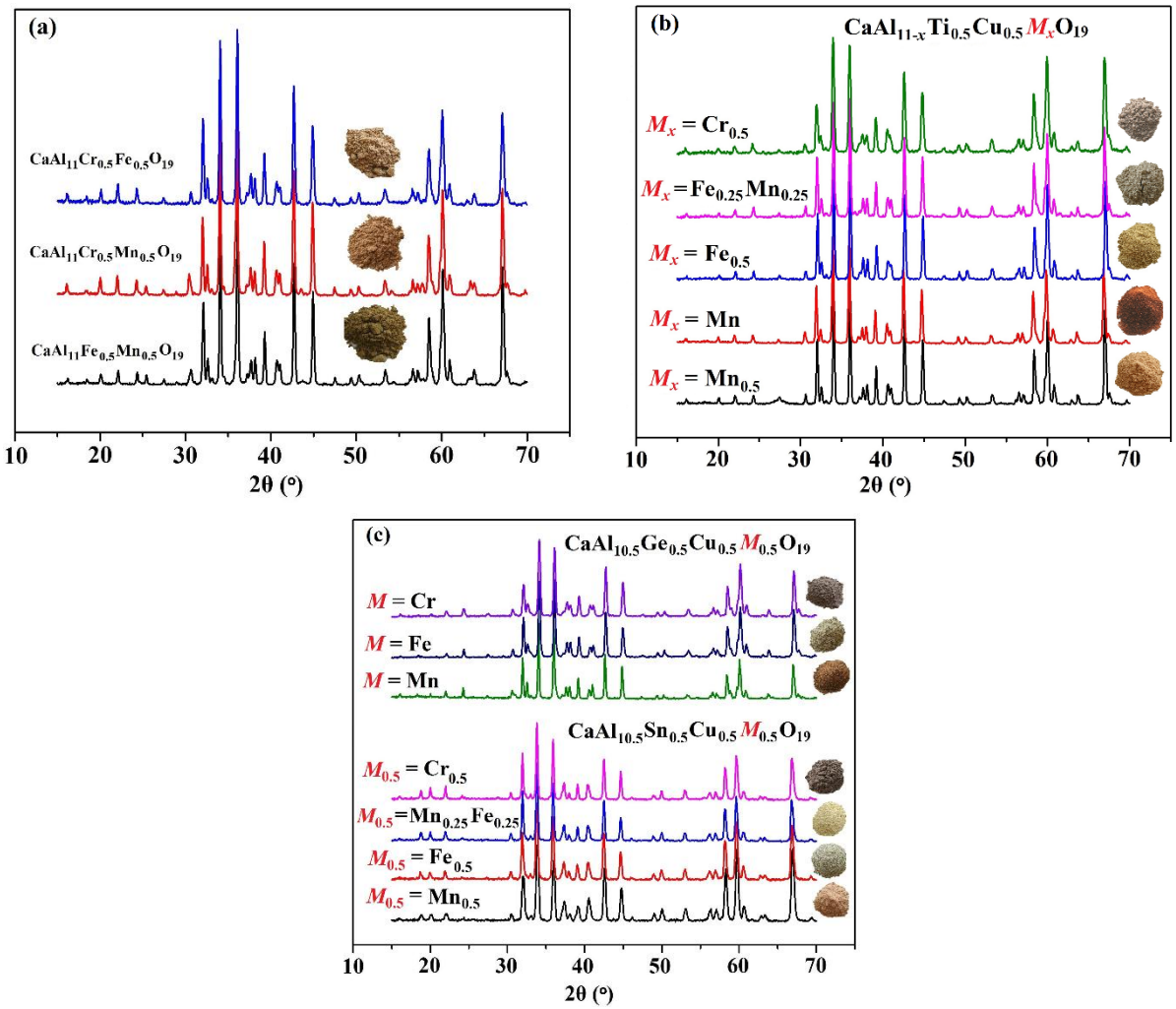

Fig. 11. XRD patterns of selected compositions: (a) $CaAl_{11}Cr_{0.5}Fe_{0.5}O_{19}$, $CaAl_{11}Cr_{0.5}Mn_{0.5}O_{19}$ and $CaAl_{11}Fe_{0.5}Mn_{0.5}O_{19}$; (b) $CaAl_{11-x}Ti_{0.5}Cu_{0.5}M_xO_{19}$ (M_x = $Cr_{0.5}$; $Fe_{0.25}Mn_{0.25}$; $Fe_{0.5}$; Mn; $Mn_{0.5}$); (c) $CaAl_{10.5}Ge_{0.5}Cu_{0.5}M_{0.5}O_{19}$ (M = Cr, Mn, Fe) and $CaAl_{10.5}Sn_{0.5}Cu_{0.5}M_{0.5}O_{19}$ ($M_{0.5}$ = $Cr_{0.5}$; $Mn_{0.25}Fe_{0.25}$; $Fe_{0.5}$; $Mn_{0.5}$).

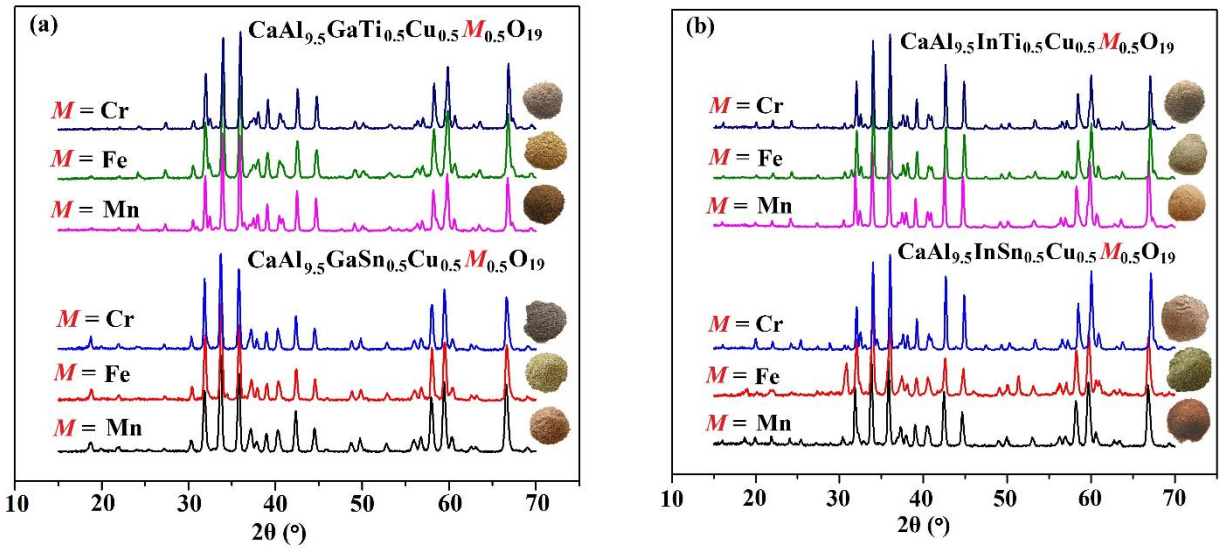

Fig. 12. XRD patterns of selected compositions: (a) $CaAl_{9.5}GaTi_{0.5}Cu_{0.5}M_{0.5}O_{19}$ (M = Cr, Fe, Mn) and $CaAl_{9.5}GaSn_{0.5}Cu_{0.5}M_{0.5}O_{19}$ (M = Cr, Fe, Mn); (b) $CaAl_{9.5}InTi_{0.5}Cu_{0.5}M_{0.5}O_{19}$ (M = Cr, Fe, Mn) and $CaAl_{9.5}InSn_{0.5}Cu_{0.5}M_{0.5}O_{19}$ (M = Cr, Fe, Mn).

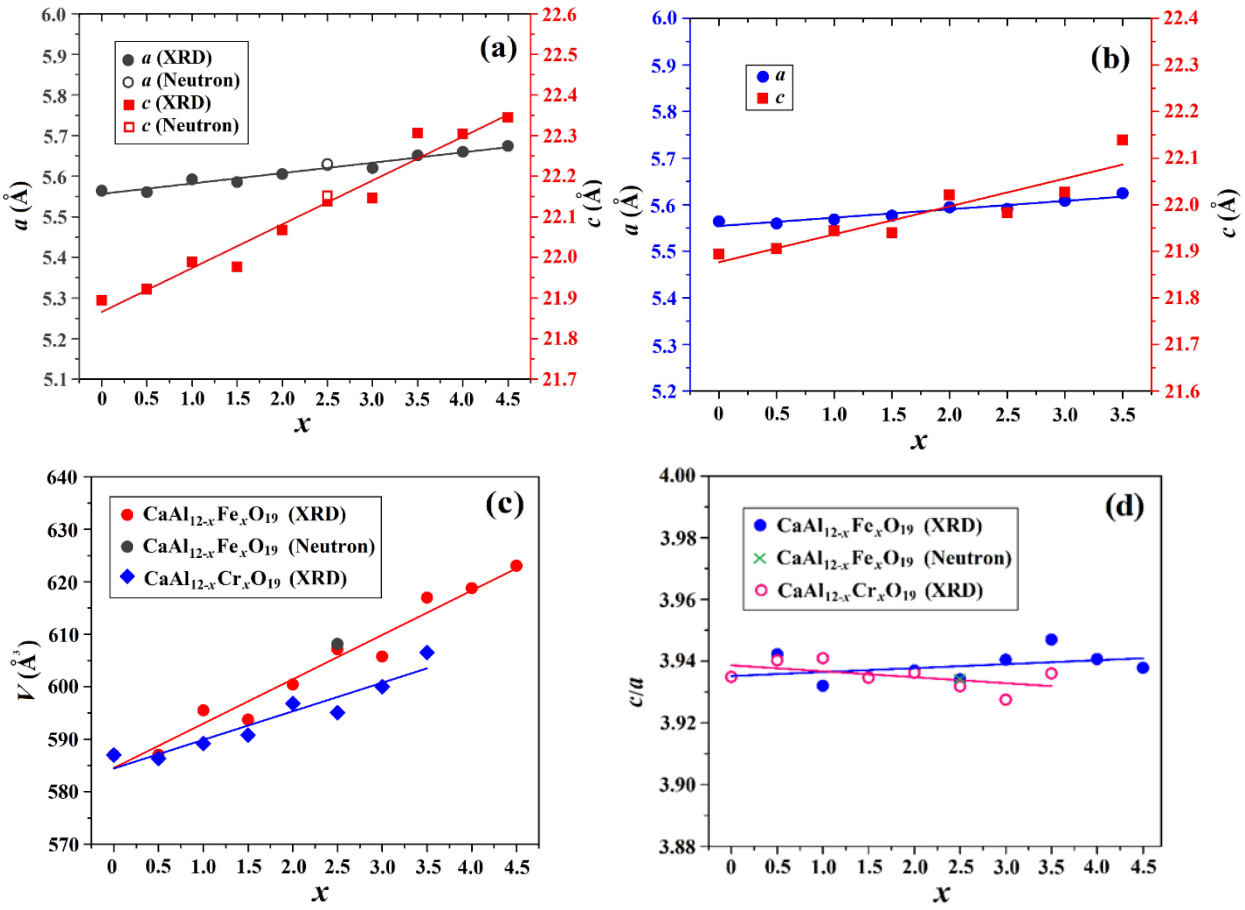

Fig. 13. Lattice parameters of $CaAl_{12-x}Fe_xO_{19}$ (x = 0.5–4.5) and $CaAl_{12-x}Cr_xO_{19}$ (x = 0.5–3.5) solid solutions: (a) cell edges a and c of $CaAl_{12-x}Fe_xO_{19}$ (x = 0.5–4.5), (b) cell edges a and c of $CaAl_{12-x}Cr_xO_{19}$ (x = 0.5–3.5), (c) cell volumes V and (d) c/a ratio as a function of x. The estimated errors for a, c and V are less than the size of the points in the figure.

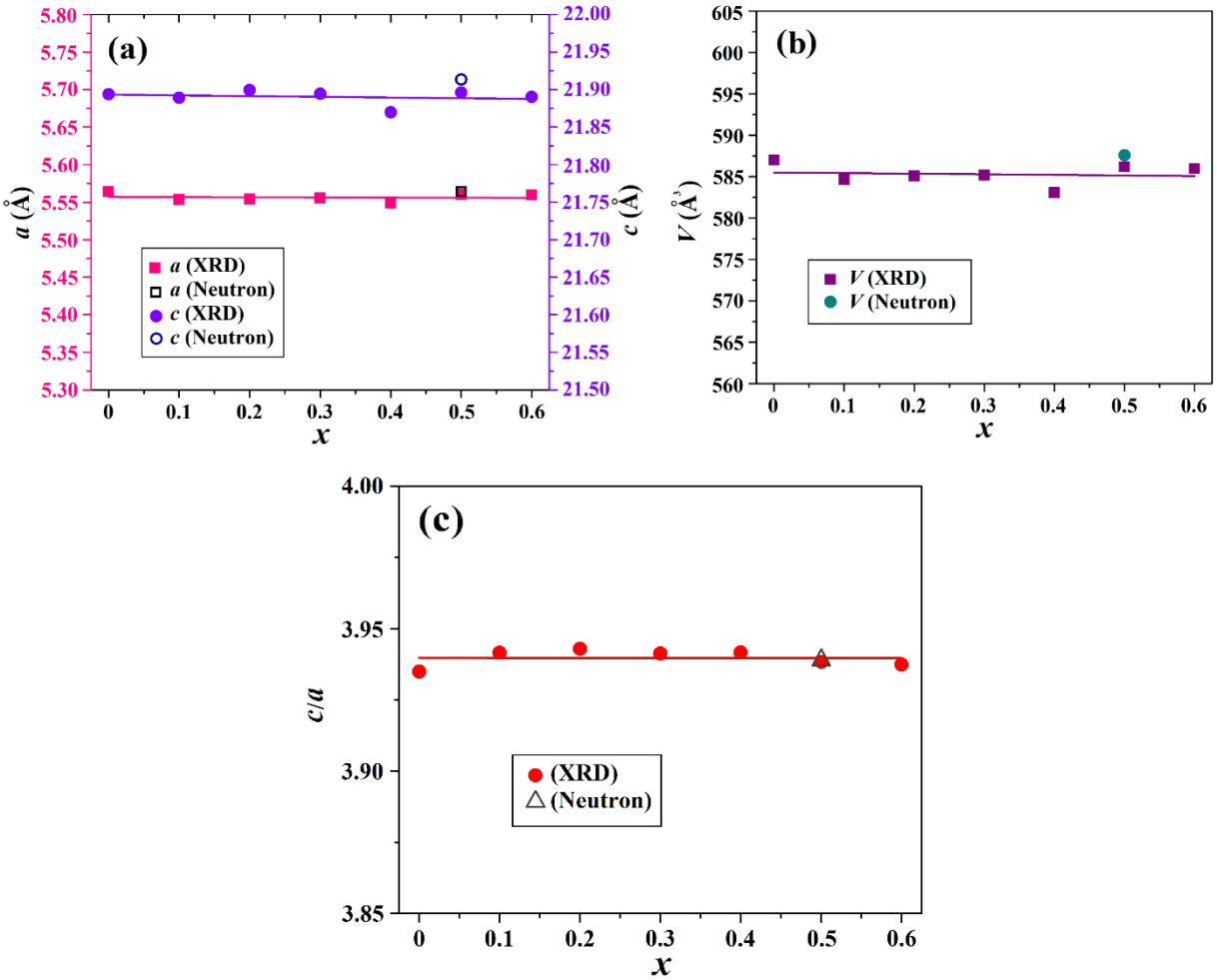

Fig. 14. Lattice parameters of $CaAl_{12-x}Mn_xO_{19}$ (x = 0.1–0.6): (a) cell edges a and c, (b) cell volume V and (c) c/a ratio as a function of x. The estimated errors for a, c and V are less than the size of the points in the figure.

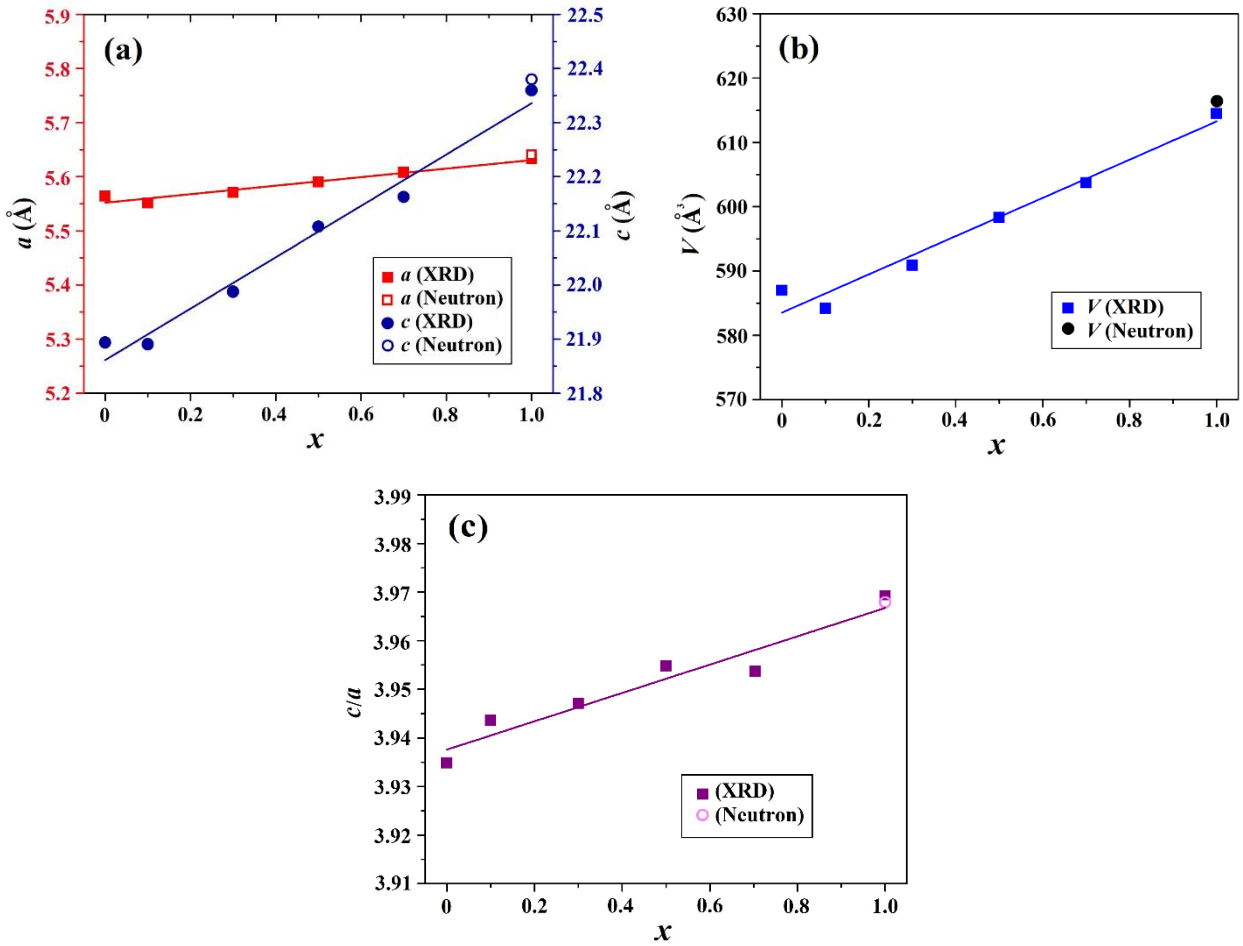

Fig. 15. Lattice parameters of $CaAl_{12-2x}Sn_xMn_xO_{19}$ (x = 0.1–1.0): (a) cell edges a and c, (b) cell volumes V and (c) c/a ratio as a function of x. The estimated errors for a, c and V are less than the size of the points in the figure.

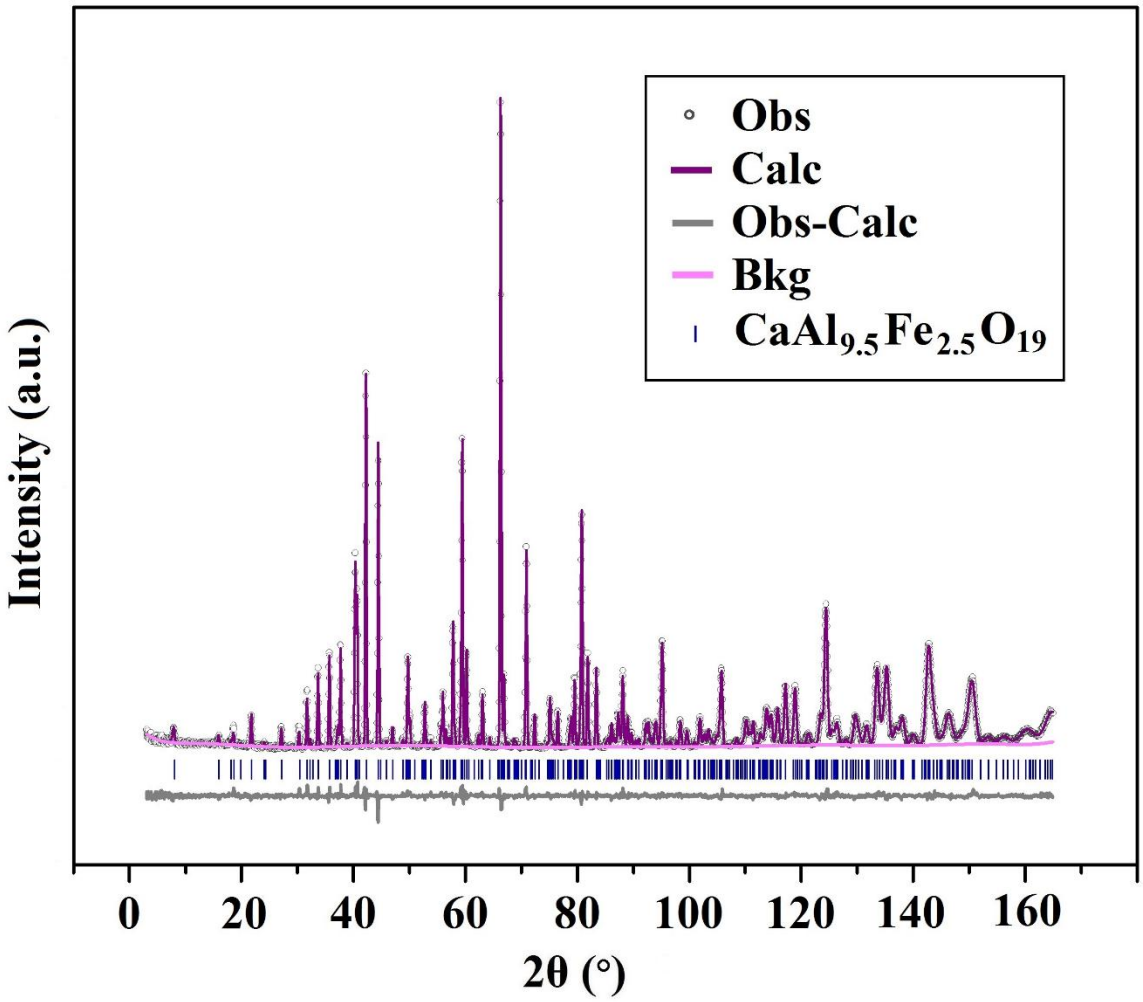

Fig. 16. Neutron data of $CaAl_{9.5}Fe_{2.5}O_{19}$ phase shown with a Rietveld fit.

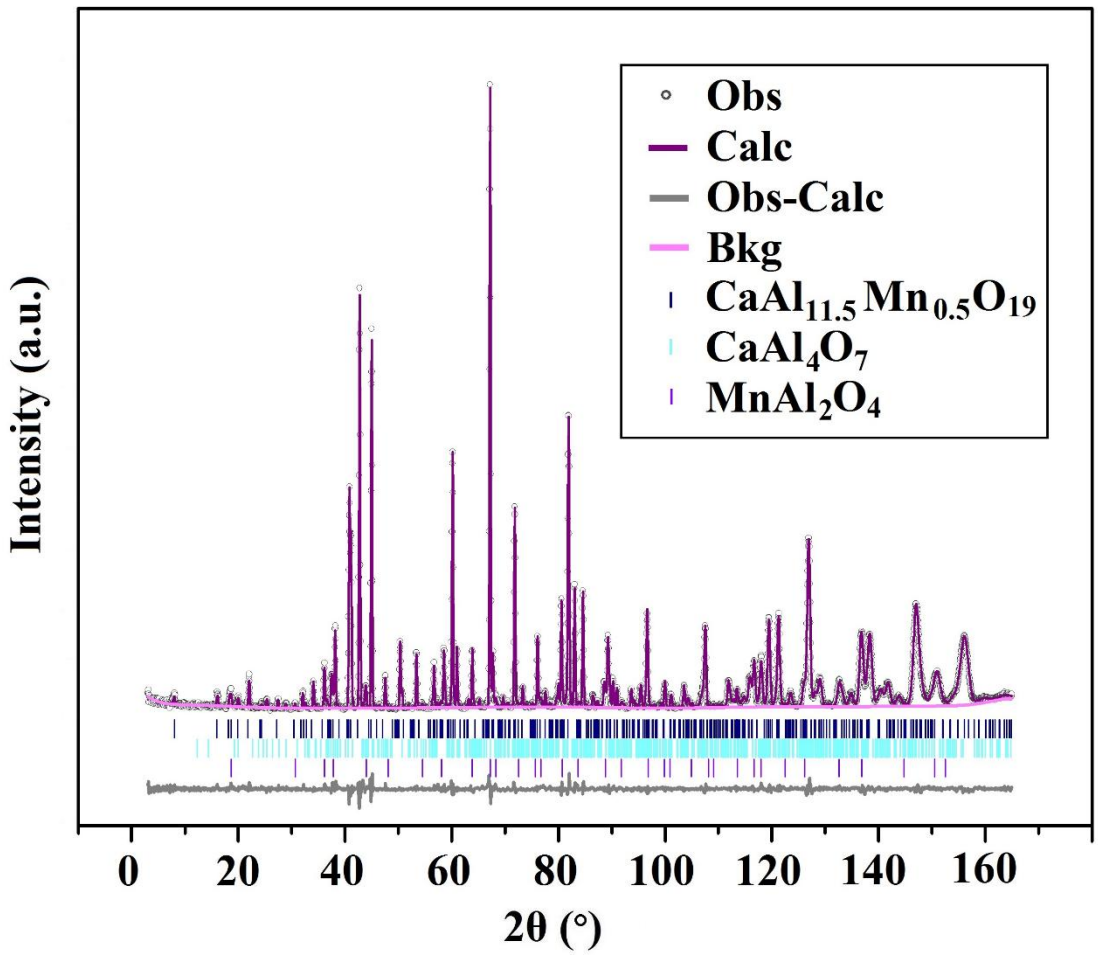

Fig. 17. Neutron diffraction data of $CaAl_{11.5}Mn_{0.5}O_{19}$ shown with a Rietveld fit. Vertical reflection lines at the bottom represent three constituent phases of the sample, from top to bottom: the major phase $CaAl_{11.5}Mn_{0.5}O_{19}$ (~91%) and two impurity phases $CaAl_4O_7$ and $MnAl_2O_4$.

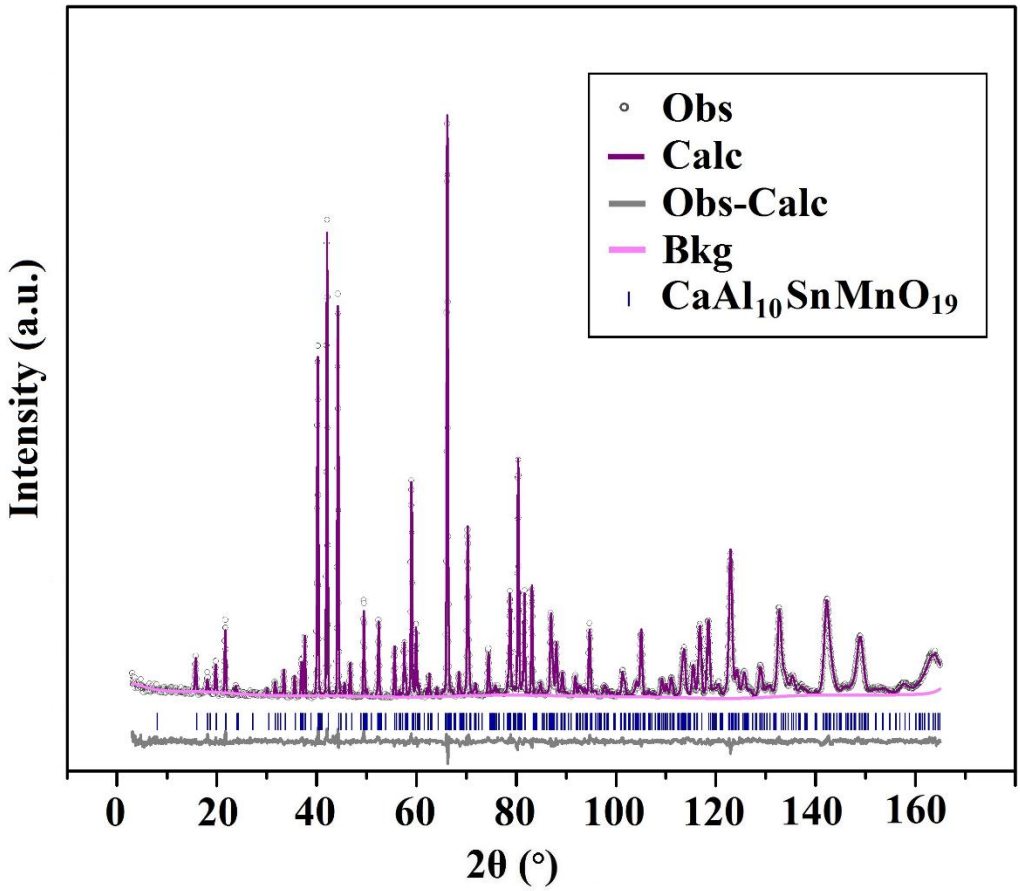

Fig. 18. Neutron data of $CaAl_{10}SnMnO_{19}$ phase shown with a Rietveld fit.

Table 2 Cell parameters by neutron Rietveld refinement.

Compound	$CaAl_{9.5}Fe_{2.5}O_{19}$	$CaAl_{11.5}Mn_{0.5}O_{19}$	$CaAl_{10}SnMnO_{19}$
a (Å)	5.6302(5)	5.5640(2)	5.6402(6)
c (Å)	22.151(5)	21.915(7)	22.379(9)
V ($Å^3$)	608.12(2)	587.57(4)	616.57(9)
R_{wp} (%)	5.16	6.00	5.96
R_p (%)	4.22	4.54	4.61
χ^2	1.45	1.76	1.59

Table 3 Refinement results of $CaAl_{9.50}Fe_{2.50}O_{19}$. The refined formula is $CaAl_{9.47}Fe_{2.53}O_{19}$.

Atoms	**Wyckoff position**	***x***	***y***	***z***	**Occupancy**	U_{iso} **(Å^2)**
Ca	2*d*	2/3	1/3	1/4	1.00	0.013(2)
Al1	2*a*	0	0	0	0.902(8)	0.006(9)
Al2	4*e*	0	0	0.2522(4)	0.321(9)	0.001(9)
Al3	4*f*	1/3	2/3	0.0285(7)	0.626(4)	0.004(9)
Al4	4*f*	1/3	2/3	0.1895(8)	0.734(5)	0.007(0)
Al5	12*k*	0.1683(2)	0.3366(4)	-0.1092(2)	0.867(7)	0.001(2)
Fe1	2*a*	0	0	0	0.098(8)	0.007(0)
Fe2	4*e*	0	0	0.2522(4)	0.178(1)	0.001(9)
Fe3	4*f*	1/3	2/3	0.0285(7)	0.374(4)	0.004(9)
Fe4	4*f*	1/3	2/3	0.1895(8)	0.266(5)	0.007(0)
Fe5	12*k*	0.1683(2)	0.3366(4)	-0.1092(2)	0.132(3)	0.001(2)
O1	4*e*	0	0	0.1481(9)	1.00	0.004(9)
O2	4*f*	1/3	2/3	-0.0556(1)	1.00	0.004(6)
O3	6*h*	0.1842(6)	0.3685(2)	1/4	1.00	0.004(5)
O4	12*k*	0.1526(8)	0.3053(7)	0.0522(1)	1.00	0.005(8)
O5	12*k*	0.5050(7)	1.0101(5)	0.1486(9)	1.00	0.006(3)

Table 4 Refinement results of $CaAl_{11.50}Mn_{0.50}O_{19}$. The refined formula is $CaAl_{11.62}Mn_{0.38}O_{19}$.

Atoms	**Wyckoff position**	***x***	***y***	***z***	**Occupancy**	U_{iso} **(Å^2)**
Ca	2*d*	2/3	1/3	1/4	1.00	0.015(5)
Al1	2*a*	0	0	0	0.983(6)	0.003(1)
Al2	4*e*	0	0	0.2590(7)	0.5	0.005(1)
Al3	4*f*	1/3	2/3	0.0276(2)	0.955(4)	0.004(2)
Al4	4*f*	1/3	2/3	0.1906(5)	0.955(5)	0.004(1)
Al5	12*k*	0.1692(8)	0.3385(6)	-0.1091(6)	0.968(9)	0.006(4)
Mn1	2*a*	0	0	0	0.017(6)	0.003(1)
Mn3	4*f*	1/3	2/3	0.0276(2)	0.045(4)	0.004(2)
Mn4	4*f*	1/3	2/3	0.1906(5)	0.045(5)	0.004(1)
Mn5	12*k*	0.1692(8)	0.3385(6)	-0.1091(6)	0.031(1)	0.006(4)
O1	4*e*	0	0	0.1494(3)	1.00	0.004(9)
O2	4*f*	1/3	2/3	-0.0553(3)	1.00	0.004(9)
O3	6*h*	0.1812(6)	0.3625(1)	1/4	1.00	0.003(6)
O4	12*k*	0.1547(2)	0.3094(3)	0.0521(3)	1.00	0.003(8)
O5	12*k*	0.5035(4)	1.0070(8)	0.1494(6)	1.00	0.003(6)

Table 5 Refinement results of $CaAl_{10}Sn_{1.0}Mn_{1.0}O_{19}$. The refined chemical formula is $CaAl_{10.31}Sn_{0.94}Mn_{0.75}O_{19}$.

Atoms	**Wyckoff position**	***x***	***y***	***z***	**Occupancy**	U_{iso} **(Å^2)**
Ca	2*d*	2/3	1/3	1/4	1.00	0.035(1)
Al1	2*a*	0	0	0	0.956(6)	0.004(2)
Al2	4*e*	0	0	0.2591(1)	0.460(4)	0.009(1)
Al3	4*f*	1/3	2/3	0.0267(8)	0.686(8)	0.066(3)
Al4	4*f*	1/3	2/3	0.1881(1)	0.651(1)	0.002(8)
Al5	12*k*	0.1672(8)	0.3345(6)	-0.1068(9)	0.960(6)	0.007(2)
Mn1	2*a*	0	0	0	0.044(6)	0.004(2)
Mn2	4*e*	0	0	0.2591(1)	0.040(4)	0.009(1)
Mn3	4*f*	1/3	2/3	0.0267(8)	0.314(8)	0.066(3)
Sn4	4*f*	1/3	2/3	0.1881(1)	0.349(1)	0.002(8)
Sn5	12*k*	0.1672(8)	0.3345(6)	-0.1068(9)	0.040(6)	0.007(2)
O1	4*e*	0	0	0.1484(7)	1.00	0.003(9)
O2	4*f*	1/3	2/3	-0.0585(4)	1.00	0.005(2)
O3	6*h*	0.1804(0)	0.3608(1)	1/4	1.00	0.005(5)
O4	12*k*	0.1500(9)	0.3001(8)	0.0525(4)	1.00	0.008(1)
O5	12*k*	0.5078(0)	1.0156(0)	0.1487(8)	1.00	0.004(4)

Table 6 Refined bond lengths (Å) and bond valence sum (BVS).

Bond distances	$CaAl_{12}O_{19}$[a]	$CaAl_{9.5}Fe_{2.5}O_{19}$	$CaAl_{11.5}Mn_{0.5}O_{19}$	$CaAl_{10}SnMnO_{19}$
6 × Ca–O3	2.7831(1)	2.8203(6)	2.7856(9)	2.823(1)
6 × Ca–O5	2.7080(9)	2.7421(5)	2.7067(9)	2.746(1)
6 × M1–O4[b]	1.8821(8)	1.8853(6)	1.8783(9)	1.8795(0)
3 × M2–O3	1.755(1)	1.7975(7)	1.7580(6)	1.7741(7)
M2–O1	2.027(5)	2.2056(3)	2.0052(8)	2.0683(6)
M2–O1’	2.384(5)	2.3048(7)	2.4028(4)	2.4761(2)
M2–O (average)[c]	**1.935**	**1.981**	**1.936**	**1.973**
3 × M3–O4	1.792(1)	1.8378(4)	1.8032(4)	1.8806(9)
M3–O2	1.823(3)	1.8647(2)	1.8179(1)	1.9094(6)
M3–O (average)	**1.800**	**1.844**	**1.807**	**1.888**
3 × M4–O5	1.871(2)	1.9040(5)	1.8723(0)	1.9182(7)
3 × M4–O3	1.956(2)	1.9760(3)	1.9595(4)	2.0372(8)
M4–O (average)	**1.914**	**1.940**	**1.916**	**1.978**
2 × M5–O5	1.809(1)	1.8169(4)	1.8071(0)	1.8443(2)
M5–O1	1.847(2)	1.8545(9)	1.8548(0)	1.8805(7)
M5–O2	1.984(2)	1.9999(4)	1.9726(5)	1.9499(9)
2 × M5–O4	1.998(1)	2.0154(5)	2.0035(4)	1.9758(2)
M5–O (average)	**1.906**	**1.920**	**1.907**	**1.912**
M2–M2[d]	0.372	0.099	0.398	0.408
M4–M4[e]	2.595	2.6768(0)	2.6013(9)	2.7701(9)
Ca, BVS	1.49	1.34	1.46	1.33

Notes.

[a]Data for $CaAl_{12}O_{19}$ are listed for comparison [56,69].

[b]M stands for Al, Fe, Mn and Sn.

[c]Average bond distances are in bold.

[d]Distances between two split sites of TBP M2.

[e]Distances between two adjacent M4 sites in face-sharing MO_6 octahedra.

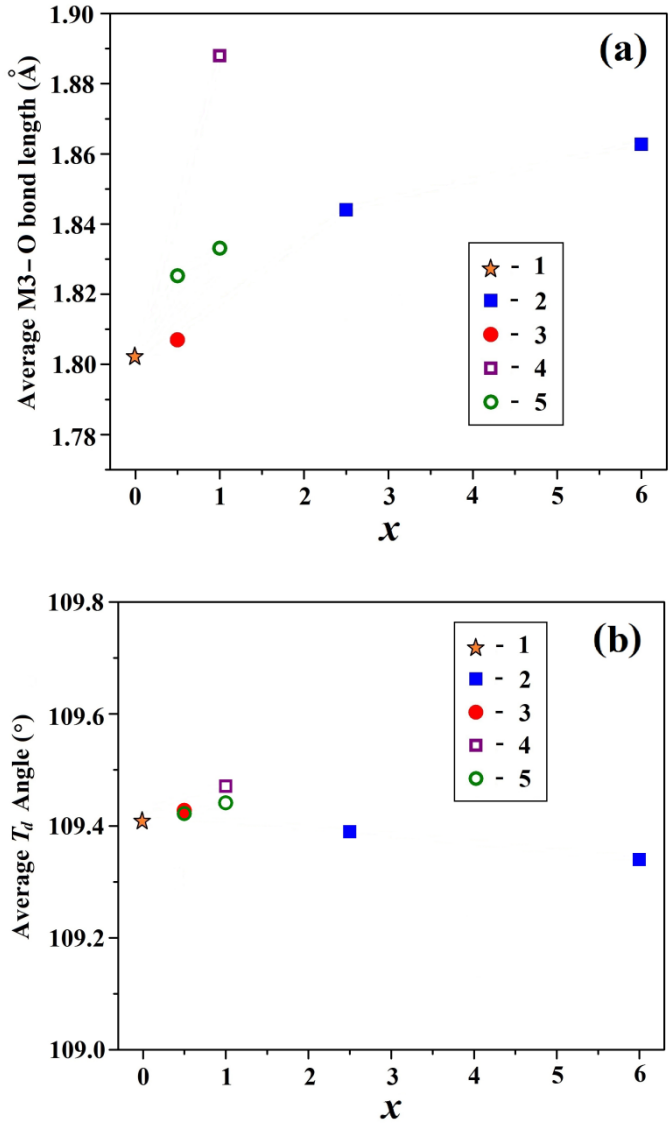

Fig. 19. Average M3–O (*M* = Al, Fe, Mn, Sn, Ni, Ti) bond lengths (a) and average bond angles (b) for tetrahedral cations in hibonite solid solutions. 1) $CaAl_{12}O_{19}$ [69]; 2) $CaAl_{12-x}Fe_xO_{19}$ (x = 2.5 this work; x = 6 from [16]); 3) $CaAl_{11.5}Mn_{0.5}O_{19}$; 4) $CaAl_{10}SnMnO_{19}$ and 5) $CaAl_{12-2x}Ti_xNi_xO_{19}$ [56,69]. The estimated error bars are less than the size of the points in the figure.

Table 7 Measured *L*a*b** values and images of colored oxides.

Chemical Formulas	*L**	*a**	*b**	Images
$CaAl_{12-x}Fe_xO_{19}$				
$CaAl_{11.5}Fe_{0.5}O_{19}$	67.22	5.87	22.33	
$CaAl_{11}FeO_{19}$	52.47	11.35	30.15	
$CaAl_{10.5}Fe_{1.5}O_{19}$	45.26	13.28	30.83	
$CaAl_{10}Fe_2O_{19}$	37.18	15.48	28.35	
$CaAl_{9.5}Fe_{2.5}O_{19}$	20.74	10.95	11.37	
$CaAl_9Fe_3O_{19}$	20.56	9.54	8.46	
$CaAl_{11-x}GaFe_xO_{19}$				
$CaAl_{10.5}GaFe_{0.5}O_{19}$	62.27	5.92	24.32	
$CaAl_{10}GaFeO_{19}$	54.93	10.88	32.08	
$CaAl_{9.5}GaFe_{1.5}O_{19}$	41.83	13.96	32.54	
$CaAl_9GaFe_2O_{19}$	25.58	12.28	16.31	
$CaAl_{12-2x}Sn_xFe_xO_{19}$				
$CaAl_{11}Sn_{0.5}Fe_{0.5}O_{19}$	64.69	0.97	14.05	
$CaAl_{10}SnFeO_{19}$	48.89	3.27	22.72	
$CaAl_9Sn_{1.5}Fe_{1.5}O_{19}$	32.00	5.79	19.98	
$CaAl_{12-2x}Ti_xFe_xO_{19}$				

$CaAl_{11}Ti_{0.5}Fe_{0.5}O_{19}$	56.87	2.62	22.13	
$CaAl_{10}TiFeO_{19}$	34.87	4.08	19.74	
$CaAl_{12-x}Mn_xO_{19}$				
$CaAl_{11.9}Mn_{0.1}O_{19}$	66.92	8.50	18.46	
$CaAl_{11.8}Mn_{0.2}O_{19}$	56.89	11.49	22.90	
$CaAl_{11.7}Mn_{0.3}O_{19}$	41.27	13.60	23.83	
$CaAl_{11.6}Mn_{0.4}O_{19}$	38.29	11.53	19.24	
$CaAl_{11.5}Mn_{0.5}O_{19}$	37.04	13.48	22.58	
$CaAl_{11.4}Mn_{0.6}O_{19}$	32.90	12.71	20.39	
$CaAl_{12-2x}Sn_xMn_xO_{19}$				
$CaAl_{11.8}Sn_{0.1}Mn_{0.1}O_{19}$	73.42	3.74	11.78	
$CaAl_{11.6}Sn_{0.3}Mn_{0.3}O_{19}$	64.83	7.81	13.87	
$CaAl_{11}Sn_{0.5}Mn_{0.5}O_{19}$	50.66	9.90	20.18	
$CaAl_{10.6}Sn_{0.7}Mn_{0.7}O_{19}$	42.34	13.17	17.87	
$CaAl_{10}SnMnO_{19}$	36.53	11.49	18.35	
$CaAl_{12-2x}Ti_xMn_xO_{19}$				
$CaAl_{11}Ti_{0.5}Mn_{0.5}O_{19}$	64.86	8.31	18.26	
$CaAl_{10}TiMnO_{19}$	34.99	11.84	18.71	

$CaAl_{11-x}Ti_{0.5}Cu_{0.5}Mn_xO_{19}$				
$CaAl_{10.5}Ti_{0.5}Cu_{0.5}Mn_{0.5}O_{19}$	57.47	10.26	23.09	
$CaAl_{10}Ti_{0.5}Cu_{0.5}MnO_{19}$	31.96	12.18	16.88	
$CaAl_{10}GeMO_{19}$				
$CaAl_{10}GeFeO_{19}$	43.16	5.21	27.35	
$CaAl_{10}GeMnO_{19}$	38.39	11.18	16.55	
$CaAl_{12-x}Cr_xO_{19}$				
$CaAl_{11.5}Cr_{0.5}O_{19}$	62.77	2.20	8.30	
$CaAl_{11}CrO_{19}$	55.88	1.35	10.52	
$CaAl_{10.5}Cr_{1.5}O_{19}$	55.33	0.29	12.52	
$CaAl_{10}Cr_2O_{19}$	48.73	-0.32	13.66	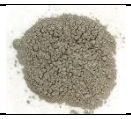
$CaAl_{9.5}Cr_{2.5}O_{19}$	46.29	-0.67	14.74	
$CaAl_9Cr_3O_{19}$	37.48	-0.42	16.12	
$CaAl_{8.5}Cr_{3.5}O_{19}$	31.97	0.13	15.15	
$CaAl_{11-x}GaCr_xO_{19}$				
$CaAl_{10.5}GaCr_{0.5}O_{19}$	58.58	1.95	9.00	
$CaAl_{10}GaCrO_{19}$	55.62	0.53	10.97	
$CaAl_{11-x}InCr_xO_{19}$				
$CaAl_{10.5}InCr_{0.5}O_{19}$	47.66	2.38	11.50	
$CaAl_{10}InCrO_{19}$	43.83	1.40	13.51	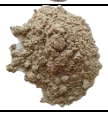

$CaAl_{12-2x}Ti_xCu_xO_{19}$				
$CaAl_{11}Ti_{0.5}Cu_{0.5}O_{19}$	72.85	2.83	9.60	
$CaAl_{10}TiCuO_{19}$	42.87	9.10	20.81	
$CaAl_9Ti_{1.5}Cu_{1.5}O_{19}$	55.29	6.27	22.25	
$CaAl_{11}M_{0.5}Cu_{0.5}O_{19}$				
$CaAl_{11}Sn_{0.5}Cu_{0.5}O_{19}$	78.11	-1.52	-0.93	
$CaAl_{11}Ge_{0.5}Cu_{0.5}O_{19}$	67.72	-1.51	2.77	
$CaAl_{9.5}GaM'_{0.5}Cu_{0.5}M''_{0.5}O_{19}$				
$CaAl_{9.5}GaSn_{0.5}Cu_{0.5}Mn_{0.5}O_{19}$	55.60	10.06	16.13	
$CaAl_{9.5}GaSn_{0.5}Cu_{0.5}Fe_{0.5}O_{19}$	58.79	1.00	20.58	
$CaAl_{9.5}GaSn_{0.5}Cu_{0.5}Cr_{0.5}O_{19}$	47.93	3.04	6.51	
$CaAl_{9.5}GaTi_{0.5}Cu_{0.5}Mn_{0.5}O_{19}$	36.53	7.68	14.24	
$CaAl_{9.5}GaTi_{0.5}Cu_{0.5}Fe_{0.5}O_{19}$	60.86	5.96	24.98	
$CaAl_{9.5}GaTi_{0.5}Cu_{0.5}Cr_{0.5}O_{19}$	33.66	2.41	6.87	
$CaAl_{9.5}InM'_{0.5}Cu_{0.5}M''_{0.5}O_{19}$				
$CaAl_{9.5}InSn_{0.5}Cu_{0.5}Mn_{0.5}O_{19}$	31.94	10.56	13.11	
$CaAl_{9.5}InSn_{0.5}Cu_{0.5}Fe_{0.5}O_{19}$	47.24	1.49	22.00	

$CaAl_{9.5}InSn_{0.5}Cu_{0.5}Cr_{0.5}O_{19}$	46.22	3.17	10.21	
$CaAl_{9.5}InTi_{0.5}Cu_{0.5}Mn_{0.5}O_{19}$	55.74	9.39	20.14	
$CaAl_{9.5}InTi_{0.5}Cu_{0.5}Fe_{0.5}O_{19}$	53.32	1.90	19.39	
$CaAl_{9.5}InTi_{0.5}Cu_{0.5}Cr_{0.5}O_{19}$	37.96	1.62	9.50	
$CaAl_{10.5}M'_{0.5}Cu_{0.5}M''_{0.5}O_{19}$				
$CaAl_{10.5}Sn_{0.5}Cu_{0.5}Mn_{0.5}O_{19}$	59.83	9.57	17.47	
$CaAl_{10.5}Sn_{0.5}Cu_{0.5}Fe_{0.5}O_{19}$	62.20	1.17	16.26	
$CaAl_{10.5}Sn_{0.5}Cu_{0.5}Cr_{0.5}O_{19}$	50.03	3.78	6.02	
$CaAl_{10.5}Ge_{0.5}Cu_{0.5}Mn_{0.5}O_{19}$	44.99	9.19	17.57	
$CaAl_{10.5}Ge_{0.5}Cu_{0.5}Fe_{0.5}O_{19}$	56.79	3.18	17.22	
$CaAl_{10.5}Ge_{0.5}Cu_{0.5}Cr_{0.5}O_{19}$	48.25	4.29	5.70	
$CaAl_{11-x}Ti_{0.5}Cu_{0.5}M_{0.5}O_{19}$				
$CaAl_{10.5}Ti_{0.5}Cu_{0.5}Fe_{0.5}O_{19}$	54.53	3.47	23.43	
$CaAl_{10.5}Ti_{0.5}Cu_{0.5}Cr_{0.5}O_{19}$	46.96	3.22	6.58	
$CaAl_{10.5}Ti_{0.5}Cu_{0.5}Mn_{0.25}Fe_{0.25}O_{19}$	55.79	3.72	15.56	
$CaAl_{10.5}Sn_{0.5}Cu_{0.5}Mn_{0.25}Fe_{0.25}O_{19}$	69.95	0.78	20.57	
$CaAl_{11}M'_{0.5}M''_{0.5}O_{19}$				

$CaAl_{11}Cr_{0.5}Fe_{0.5}O_{19}$	51.47	5.12	15.47	
$CaAl_{11}Cr_{0.5}Mn_{0.5}O_{19}$	43.43	8.11	16.58	
$CaAl_{11}Fe_{0.5}Mn_{0.5}O_{19}$	41.47	6.65	17.88	

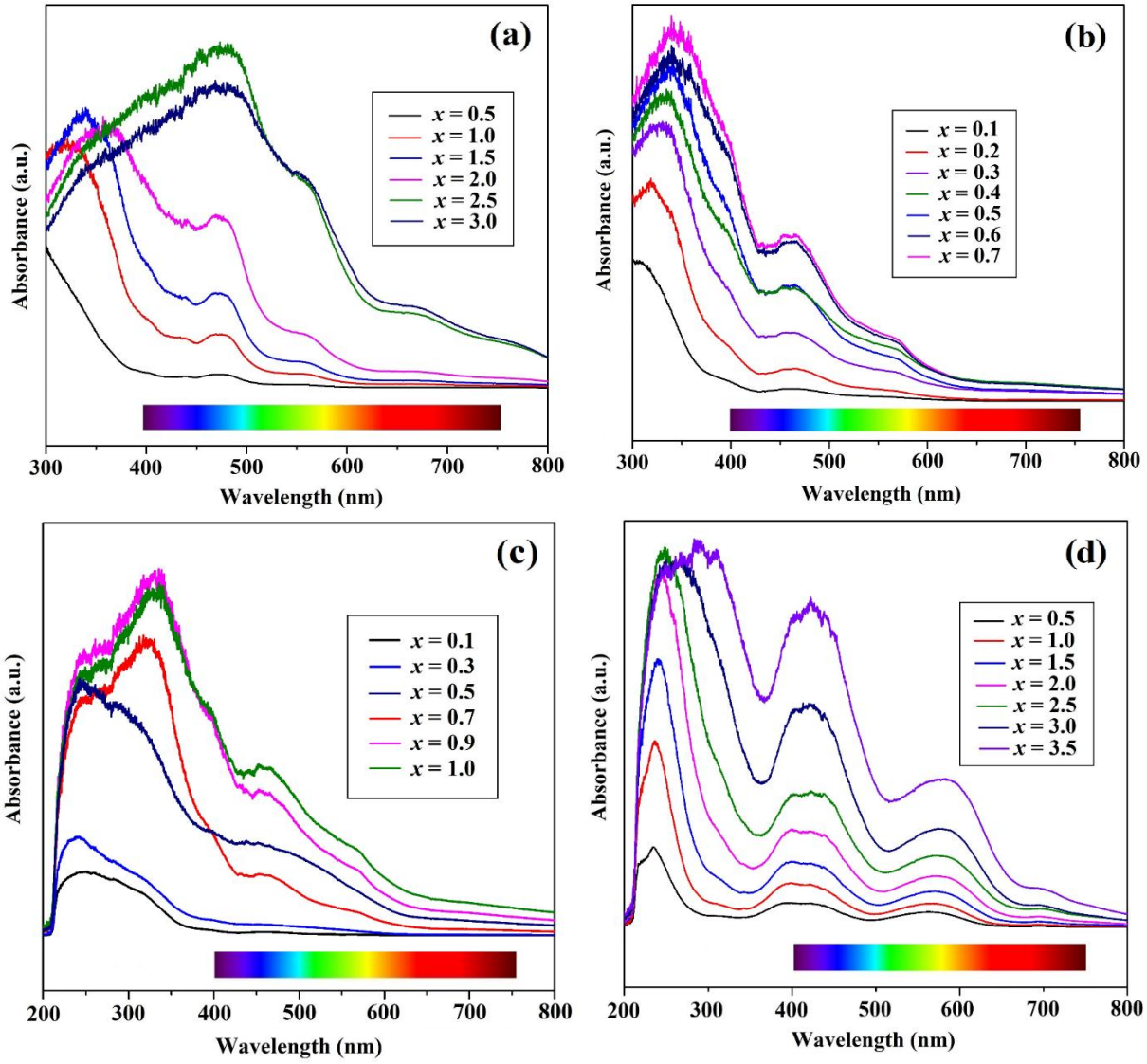

Fig. 20. Diffuse reflectance spectra as a function of wavelength (nm): (a) $CaAl_{12-x}Fe_xO_{19}$ (x = 0.5–3.0), (b) $CaAl_{12-x}Mn_xO_{19}$ (x = 0.1–0.6), (c) $CaAl_{12-2x}Sn_xMn_xO_{19}$ (x = 0.1–1.0) and (d) $CaAl_{12-x}Cr_xO_{19}$ (x = 0.5–3.5) solid solutions.

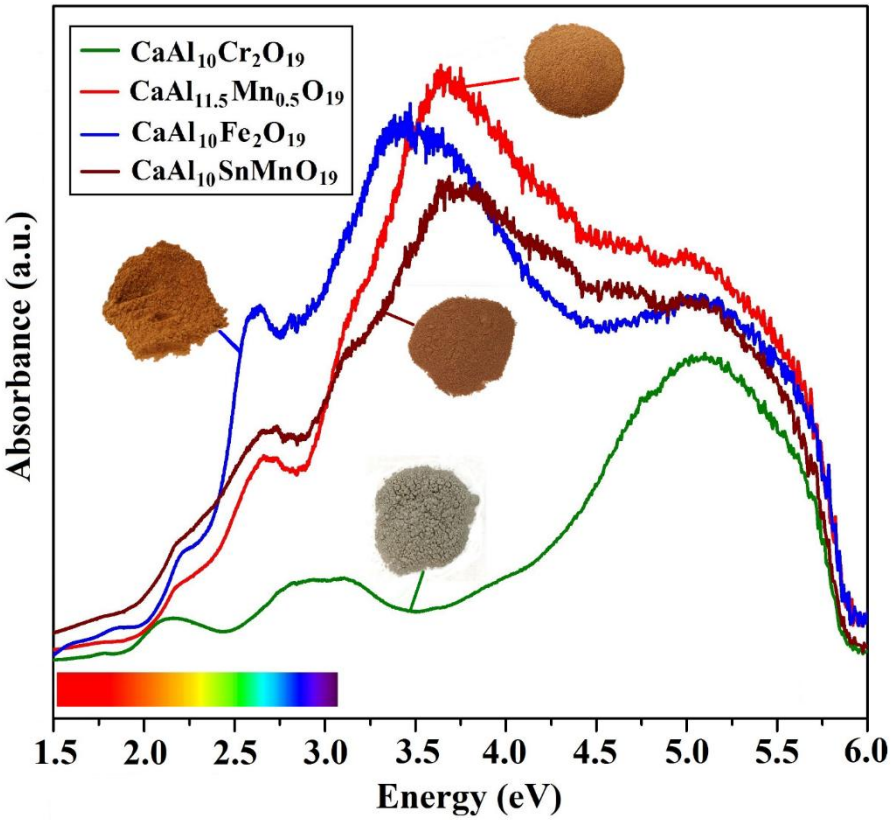

Fig. 21. Diffuse reflectance spectra of $CaAl_{10}Fe_2O_{19}$, $CaAl_{11.5}Mn_{0.5}O_{19}$, $CaAl_{10}SnMnO_{19}$ and $CaAl_{10}Cr_2O_{19}$ as a function of photon energy (eV).

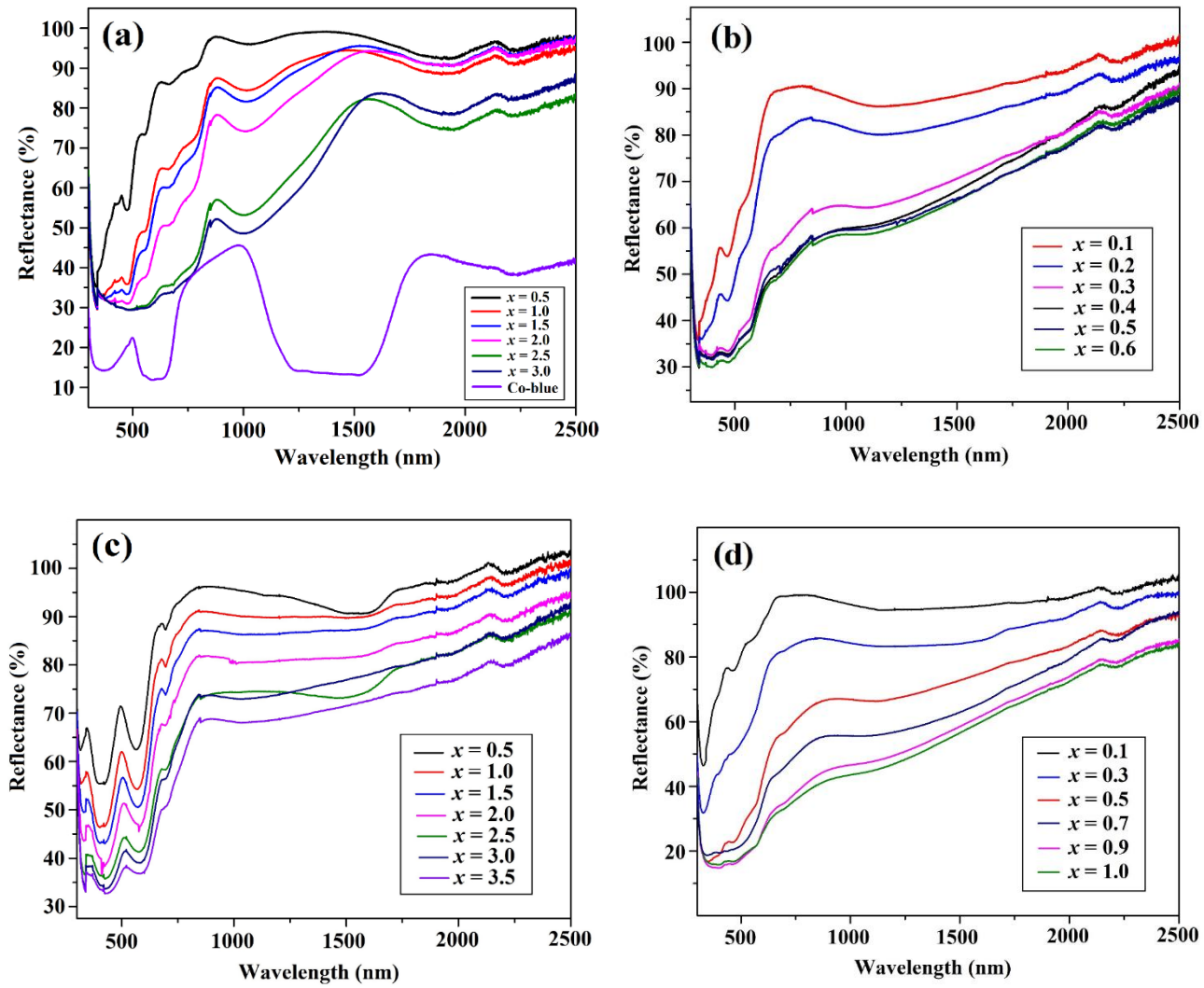

Fig. 22. UV-Vis and NIR reflectance of (a) $CaAl_{12-x}Fe_xO_{19}$ (x = 0.5–3.0) and commercial Co-blue, (b) $CaAl_{12-x}Mn_xO_{19}$ (x = 0.1–0.6), (c) $CaAl_{12-2x}Sn_xMn_xO_{19}$ (x = 0.1–1.0) and (d) $CaAl_{12-x}Cr_xO_{19}$ (x = 0.5–3.5) solid solutions.

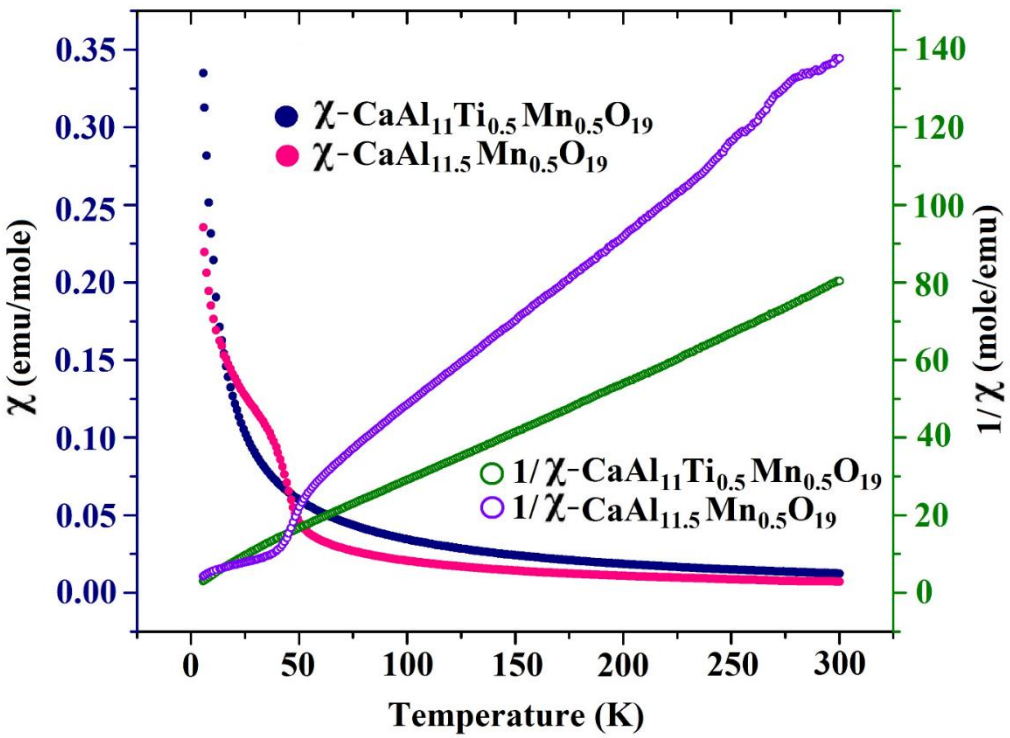

Fig. 23. Magnetic susceptibility and inverse magnetic susceptibility of $CaAl_{11.5}Mn_{0.5}O_{19}$ and $CaAl_{11}Ti_{0.5}Mn_{0.5}O_{19}$ as a function of temperature. 1 emu (cgs units) = 10^{-3} A m^2 (SI units).

Table 8 Calculated magnetic moments, Curie and Weiss constants of $CaAl_{11.5}Mn_{0.5}O_{19}$ and $CaAl_{11}Ti_{0.5}Mn_{0.5}O_{19}$ samples.

Compound	T (K)	C	θ (K)	μ_{eff} (μ_B)
$CaAl_{11.5}Mn_{0.5}O_{19}$	250-300	2.4307	-28.10	4.43
$CaAl_{11}Ti_{0.5}Mn_{0.5}O_{19}$	250-300	3.8270	-1.050	5.56

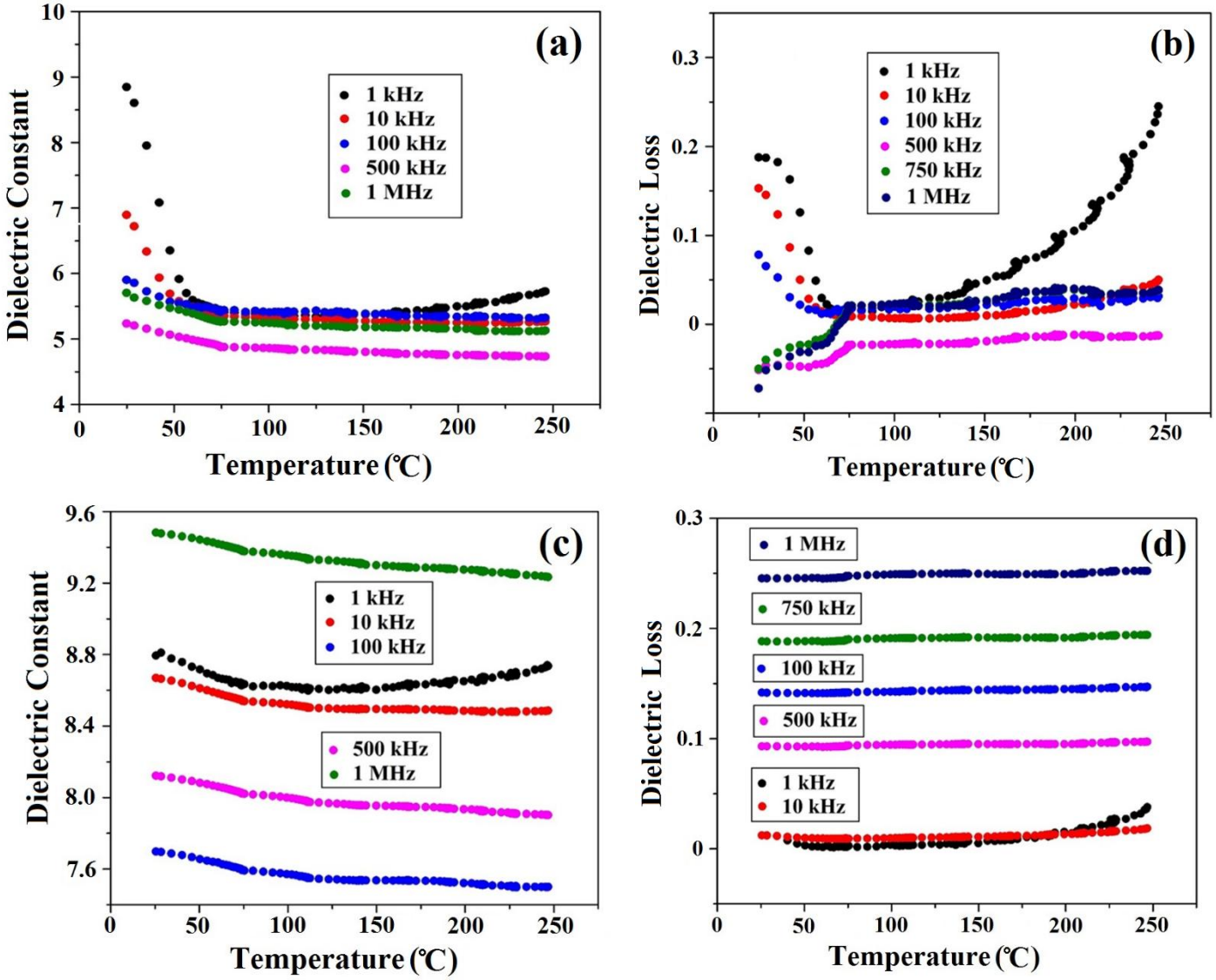

Fig. 24. Dielectric constant κ and dielectric loss as a function of temperature: (a, b) $CaAl_{11.5}Fe_{0.5}O_{19}$; (c, d) $CaAl_{11.4}Sn_{0.3}Mn_{0.3}O_{19}$.

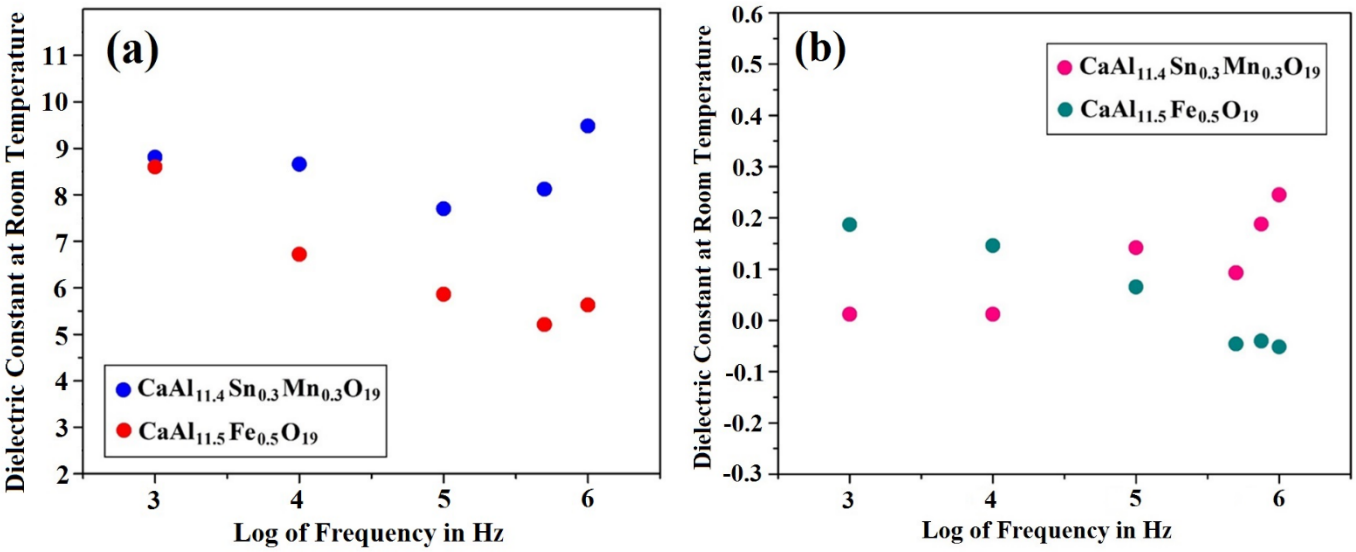

Fig. 25. Frequency dependence of (a) dielectric constant and (b) dielectric loss of $CaAl_{11.5}Fe_{0.5}O_{19}$ and $CaAl_{11.4}Sn_{0.3}Mn_{0.3}O_{19}$ at room temperature.

Graphical Abstract for the Table of Contents (TOC)

Colored hibonite oxides with Fe, Mn and Cr as chromophores.